

# **A Numerical Analysis of Graphene based D-shaped plasmonic sensor for multi-analyte detection**

(This thesis report has been submitted in partial fulfillment of the requirements for the degree of Bachelor of Science in Electrical and Electronic Engineering)

## **Submitted by**

Rakib Haider: 183-33-4825  
Md. Obaidullah bin Masum: 183-33-4787

## **Supervised by**

DR. Md. Rezwanul Ahsan  
Associate Professor  
Department of Electrical and Electronic Engineering



Department of Electrical and Electronic Engineering

Faculty of Engineering

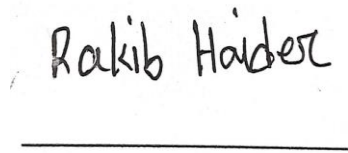
DAFFODIL INTERNATIONAL UNIVERSITY

JANUARY, 2023

## DECLARATION

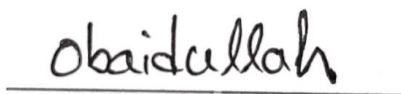
I am familiar with Daffodil International University's anti-plagiarism policies. To the best of my knowledge and belief, the work submitted here is my original creation and contains no material that has been published or written by another person or that has been accepted for the award of any other degree or diploma of the university or other institute of higher learning, except where proper citation has been made.

### Signature of the candidates

  
\_\_\_\_\_

Name: Rakib Haider

ID: 183-33-4825

  
\_\_\_\_\_

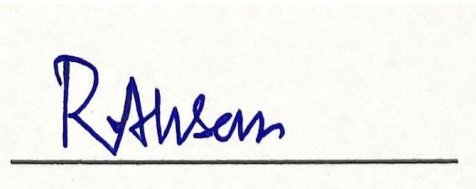
Name: Obaidullah Bin Masum

ID: 183-33-4787

## Approval

The project entitled “A Numerical Analysis of Graphene based D-shaped plasmonic sensor for multi-analyte detection” submitted by **Rakib Haider & Obaidullah Bin Masum** has been done under my supervision and accepted as satisfactory in partial fulfillment of the requirements for the degree of **Bachelor of Science in Electrical and Electronic Engineering** in **January, 2023**.

### Signature of the supervisor

A handwritten signature in blue ink, reading "R. Ahsan", is written over a horizontal line on a light-colored background.

DR. Md. Rezwatul Ahsan

Associate Professor

Department of Electrical and Electronic Engineering

Faculty of Engineering

Daffodil International University

## ACKNOWLEDGEMENT

First of all, we want to give thanks to **Almighty Allah**. With his blessing we are able to complete our work with best effort.

We want to pay our utmost respect to our Supervisor **DR. Md. Rezwanul Ahsan**, Associate Professor of the **Department of EEE, Daffodil International University** for who has given us the chance to work on an impactful idea and taken care of every issue of development of this concept. Then we would like to take this opportunity to express gratitude to our supervisor for being dedicated in supporting, motivating and guiding us throughout this project. This project can't be done without his useful advice and help. Also thank him very much for giving us the opportunity to work with this project.

## ABSTRACT

Since decades ago, the PCF-based surface plasmon resonance (SPR) sensor has attracted increased attention due to its unique properties, including compact size, simple light transmission via the fiber core, control over light propagation, design flexibility, and excellent sensing ability. The D-shaped PCF-based SPR sensing phenomenon is extensively employed in sensing applications for liquid detection, chemical detection, and biomolecular interaction in medical diagnostics. Although the D-shaped PCF based SPR sensor demonstrates great sensitivity, its main limitation is the requirement for deep polishing depth, which makes fibers more fragile in the manufacturing environment. This thesis investigates how to enhance existing PCF sensors based on SPR and how to employ a better understanding of their physical and sensing principles to suggest new design concepts and ideas with smaller polishing depth. A systematic approach was used to look at several structural factors, such as the location, optical characteristics, shape, and thickness of the metal components, that might affect how well a sensor performs. In this paper, we have proposed a graphene embedded photonic crystal fiber (PCF) based surface plasmon resonance (SPR) sensor for multi-analyte detection simultaneously. The graphene layer improves the sensing performance due to their high surface to volume ratio. The proposed sensor is numerically investigated where channels are coated with gold and graphene layers. Top and bottom side of the fiber etched down to make it double sided D-shape. The double D-shaped structure works based on external sensing mechanism and facilitate to utilize the multi-analyte detection approach. The proposed fiber consists with six air holes, and two of them are used as fiber cores by filling up with the high refractive index (RI) liquid of 1.46. The fiber is fabricated using stack-and-draw fiber fabrication method. The finite element method (FEM) approach is used to investigate the fiber's characteristics and sensing performance numerically. Due to asymmetry of the fiber structure, the proposed sensor demonstrates polarization dependency and exhibits sensing phenomena for the x-polarized mode. The sensor can detect the unknown analyte RI at the detection range of 1.32 to 1.42. The sensing range is separated into two groups such as Ch-1 (RI from 1.32 to 1.37) and Ch-2 (RI from 1.38 to 1.42) to demonstrate multi-analyte detection phenomena. The proposed sensor exhibits the maximum wavelength and amplitude sensitivities of 14,000 nm/RIU and 1922 RIU<sup>-1</sup>, respectively. Also, the effects of structural parameters on the sensor performance, such as graphene layer thickness, gold layer thickness, air

holes, fused silica, and diameter are numerically investigated. Consequently, we may anticipate that the demonstrated sensor with multi-analyte detection capacity will make it more promising choice for medical diagnostics, biochemical, and organic chemical detection.

Keywords:

**Photonic Crystal Fiber, Optical Fiber, Surface Plasmon, Surface Plasmon Resonance, Finite Element Method, Biosensor, Micro-structured Optical Fiber, Refractive Index Sensor**

# TABLE OF CONTENTS

DECLARATION.....	ii
APPROVAL.....	iii
ACKNOWLEDGEMENT.....	iv
ABSTRACT.....	v
TABLE OF CONTENTS.....	vii
LIST OF TABLES.....	ix
LIST OF FIGURES.....	ix
LIST OF ABBREVIATIONS.....	xi
CHAPTER 1: INTRODUCTION.....	1
1.1 Introduction.....	1
1.2 Motivation.....	2
1.3 Problem statement.....	3
1.4 Objectives.....	3
CHAPTER 2: LITERATURE REVIEW AND TECHNICAL BACKGROUND.....	4
2.1 overview.....	4
2.2 Surface Plasmon and Surface Plasmon Resonance.....	4
2.2.1 Surface plasmon.....	4
2.2.2 Surface Plasmon Resonance.....	5
2.3 Surface plasmon resonance sensing technique.....	6
2.3.1 conventional Prism based SPR Configuration.....	6
2.3.2 Photonic crystal fiber surface plasmon resonance.....	8
2.4 Fiber Optic Technology.....	9
2.4.1 Conventional optical fiber.....	9
2.4.2 Photonic crystal fiber.....	10
2.5 PCF Structure Implementation.....	11
2.5.1 Geometrical definition.....	11
2.5.2 Background material.....	12
2.6 Performance Analysis Parameters.....	12
2.7 Literature Review on PCF based SPR Sensors.....	14
CHAPTER 3: METHODOLOGY.....	18

3.1	Introduction.....	18
3.2	Design Structure.....	18
3.3	Boundary setting .....	19
3.4	Messing.....	20
3.5	Plasmonic Materials for the Proposed Sensor .....	21
3.6	Research Model .....	22
3.7	Numerical Tools.....	22
CHAPTER 4: RESULT AND DISCUSSION.....		24
4.1	Introduction.....	24
4.2	Multi-analyte Sensing.....	24
4.3	Single-analyte sensing .....	28
4.4	Sensor tolerance & optimization.....	31
CHAPTER 5: CONCLUSION AND FUTURE WORK.....		34
5.1	Conclusion .....	34
5.2	Limitation.....	34
5.3	Future Work .....	35



## LIST OF TABLES

Table 1: Table 1. Performance information of the proposed multi-analyte operation.....	26
Table 2: Table 2. Performance information of the proposed single analyte operation.....	28
Table 3: Performance comparison of the proposed double D-shaped plasmonic sensor for multi-analyte detection.....	31

## LIST OF FIGURES

Figure 1.1: Variety areas of PCF based SPR sensor.....	02
Figure 2.1: Plasmon oscillation in the metal.....	05
Figure 2.2: Localized SPR when field (light) interacts with the plasmons.....	06
Figure 2.3: Otto-configuration for SPR sensor.....	07
Figure 2.4: Kretschmann configuration for SPR sensor .....	08
Figure 2.5: Conventional Optical fiber structure .....	10
Figure 2.6: Multimode and Single-mode optical fiber .....	10
Figure 2.7: (a) Hollow core fiber cross section (b) Solid core fiber cross-section .....	11
Figure 2.8: (a)Cross-section of hexagonal ( $60^{\circ}$ angle) PCF, (b) Cross-section view of octagonal ( $45^{\circ}$ angle) PCF, (c) cross-section view of decagonal ( $36^{\circ}$ angle) PCF.....	11
Figure 2.9: Figure 2.9: (a) & (b) Cross-section view of the sensor and selective air hole metal coating.....	15
Figure 2.10: Figure 2.10: Cross section view of external sensing approach (a) Rectangular core based PCF sensor (b) spiral PCF sensor (c) Schematic of the designed exposed-core grapefruit fiber based SPR sensor (d) microfluidic slotted based sensor for multi-analytes detection.....	16

Figure 2.11: (a) A microchannel based D-shaped PCF sensor (b) D-type PCF based SPR sensor for sensing analyte RI and temperature.....	17
Figure 3.1: (a) Figure 3.1 (a) a cross-sectional 2D view of the PCF sensor. (b) Verification of multianalyte operation feasibility.....	19
Figure 3.2: PML boundary layer.....	20
Figure 3.3: Mesh.....	21
Figure 3.4: Basic simulation layout for the proposed sensor.....	22
Figure 4.1: Distribution of X-polarized electric fields of core-guided mode and SPP mode (a & c) at analyte RI 1.36 for channel 1 and (c & d) at analyte RI 1.41 for channel 2.....	35
Figure 4.2: (a) Y-polarized phase-matching condition when channel 1 is filled with RI 1.36 liquid, and channel 2 is filled with RI 1.42 liquid, (b) Birefringence character of the sensor.....	24
Figure 4.3: For multi-analyte detection, (a) right shift of SPR with any increase in RI of the infiltrated liquid, (b) amplitude sensitivities for different RIs.....	26
Figure 4.4: (a) Loss peaks and 2nd order polynomial fitting of the resonant wavelength with respect to RI, (b) the relation between FOM and FWHM at individual RI.....	27
Figure 4.5: (a) phase matching at RI 1.41 (b) Birefringence character of the sensor.....	29
Figure 4.6: For single analyte sensing while both channels are filled by the same analyte (a) Loss spectrum with the change of analyte RI variation from $n_a = 1.33$ to 1.42, and (b) amplitude sensitivities.....	30
Figure 4.7: (a) Loss curves resulted from gold layer thickness variation and (b) relevant amplitude sensitivities.....	31
Figure 4.8: Tolerance investigation by changing (a) pitch size ( $\Lambda=2.028\mu\text{m}$ ) and (b) airholes diameter ( $d=1.95\mu\text{m}$ ).....	32
Figure 4.9: (a) Graphene layer variation of RI 1.40 (b) Amplitude sensitivity of Graphene layer..	33

## LIST OF ABBREVIATIONS

PCF	:	Photonic Crystal Fiber
SPR	:	Surface Plasmon Resonance
SPW	:	Surface Plasmon Wave
SP	:	Surface Plasmon
SPP	:	Surface Plasmon Polariton
MOF	:	Microstructured optical fiber
RIU	:	Refractive Index Unit
RI	:	Refractive Index
CVD	:	Chemical Vapor Deposition
NIR	:	Near-infrared Region
EMI	:	Electromagnetic Interference
TIR	:	Total Internal Reflection
SEM	:	Scanning Electron Microscopy
TE	:	Transverse Electric
TM	:	Transverse Magnetic
FEM	:	Finite Element Method
MM	:	Multipole Method

# CHAPTER 1: INTRODUCTION

## 1.1 Introduction

Researchers have made significant efforts in recent decades to research the surface plasmon resonance (SPR) phenomena both experimentally and conceptually. Surface plasmons are created when the free electrons on a surface of the metal collectively oscillate in response to a waveform. This resonant interaction is what gives rise to surface plasmons. After then, Surface plasmon are intensely bounded on the metal-dielectric interface, leading to an increase in the electric field strength[1]. Additionally, the SP effect also has the unique quality of being highly sensitive to little changes in refractive index. Since 1996, PCFs have received widespread optical transmission[2]. According to experts, Light propagation in PCFs may be controlled by enclosing micro-nano size air gaps in the shape of photonic crystals, since photonic crystals can affect electromagnetic waves of a given wavelength in a fiber. PCFs' superior design flexibility means that their dispersion, birefringence, nonlinearity may be fine-tuned by modifying the air pore configuration[3]. PCFs' superior design flexibility means that their dispersion, birefringence, nonlinearity may be fine-tuned by modifying the air pore configuration. These features make PCFs extremely appealing in a variety of contexts, leading to many applications in areas such as gas-based nonlinear optics, atom and particle guiding, ultrahigh nonlinearities, rare-earth doped lasers, and sensing fields[4]. Currently, Stack-and-Draw method is the most widely used method of PCF fabrication as it has proven to be mature and highly flexible in assembling complex meshes from stackable units of acceptable size and form[5]. This method also enables the simple inclusion of solid, bare, or doped glass. PCFs include intrinsic microstructure channels that allow for the infiltration or selective infiltration of functional materials (gas, solid, or liquid) to modify light-matter interactions. Additionally, PCFs may also be processed similarly to regular optical fibers using techniques including by side polishing, rotation, slots, and coating technologies; this significantly broadens PCFs' potential uses[6].

Although the first SPR-based biosensor, a prism-based device, was developed in 1983 for biological applications and released commercially in 1990[7], the technology has since undergone significant development. Prism-based SPR sensors have several drawbacks, including bulkiness, a few numbers of acceptance angles, and poor real-time remote sensing performance [8]. To overcome all of the drawbacks of traditional prism-based SPR, a PCF-

based SPR sensor has been developed[9]. The PCF-based SPR sensor has characteristics like compact size, high sensing accuracy, extensive detection range, and design flexibility[10]. It is a combination of plasmonic materials with photonic crystal fiber technology.

When using a photonic crystal fiber (PCF) for SPR, light travels down the fiber's core and creates an evanescent field as it exits the cladding [11]. The SPR generated by the coupling of the evanescent field with the metal layer is useful for the detection of previously undetected analytes. It was reported in 1993 that surface plasmon resonance may be used in a fiber-optic chemical sensor[12].

## 1.2 Motivation

Prism coupling-based biosensors are widely employed due to their ease of use. However, it is heavy and contains moving optical and mechanical parts, which limits its application in remote sensing. In contrast, PCF offers design flexibility, small size and lightweight can be used for remote sensing applications, and exhibits birefringence, low confinement loss, nonlinearity, etc. Consequently, PCF replaced prism-based SPR sensing techniques where prisms were bulky and hard to fix the angle of incidence of light. In addition, PCF-based SPR sensors exhibit more sensitivity than prism-based SPR sensors. Furthermore, a small change in the RI of an analyte may be detected by observing a shift in 4 major peak wavelengths. That's why surface plasmon resonance biosensors based on photonic crystal fibers are the most effective and versatile option. To see where PCF-based SPR sensors are most often and extensively employed, refer to Fig1.1.



**Fig 1.1:** Variety areas of PCF based SPR sensor [13].

### 1.3 Problem statement

Numerous reports have been made on PCF-based SPR sensors so far. In spite of this, most suggested designs are very complicated and difficult to fabricate. Some issues that may arise include the metal layer coating of selective holes and liquid penetration into selective air holes, both of which increase hole size to roughly 1-2  $\mu\text{m}$  [14]. Internal sensing, exterior sensing, and the D-shaped sensing approach are the three broad categories into which all published PCF based SPR sensor investigations may be sorted in order to examine the sensing performance [15]. The internal sensing technique is quite complicated because it needs coating the inner surface of selected holes (typically a few nm and up to 1-2  $\mu\text{m}$  in diameter) with metals and infiltrating the sensing analyte (or liquid) into selective holes[16]. All the metallic coating and analyte may be applied outside, making the external sensing technique more straightforward than the internal sensing approach[17]. The major issue with D-shaped PCF is that the gap between the metal layers must be decreased to only a few micrometers by polishing about half of the fiber structure, at which point the fiber becomes exceedingly brittle[18]. In addition to the aforementioned issues, most PCF-based SPR sensors are designed with very small air holes ranging from about a few nm to 1-2  $\mu\text{m}$  in diameter, which is also complicated in practice. Another challenge is that D-shaped sensors require very precise polishing to accurately obtain the micron distance between the D-surface and the core, as well as a very flat and smooth surface[19].

- How to make a PCF based SPR sensor with higher sensitivity by external sensing approach?
- How to reduce the polishing depth of the fiber compared to the conventional D-shaped fibers?

### 1.4 Objectives

The internal sensing strategy is challenging to manufacture, while the exterior sensing approach has limited sensitivity. Additionally, current D-shaped PCF sensors have great sensitivity but need deep polishing, which weakens the fiber. Since ordinary D-shaped fibers need more polishing depth, the goal of this work is to build an external sensing PCF-based SPR sensor with improved sensitivity. In specific, the objectives of this study are:

- i) To design a PCF structure suitable for SPR external sensing that provides higher sensitivity but requires smaller polishing depth.
- ii) To evaluate performance of the proposed sensor by simulation.

## **CHAPTER 2: LITERATURE REVIEW AND TECHNICAL BACKGROUND**

### **2.1 overview**

SPR sensing technique are widely used for sensing which is works based on interaction on light coupling at a dielectric metal surface. This chapter provides a comprehensive overview of SPR phenomena, the methodology behind standard prism-based SPR sensors, and the issues that arise from using them. The fundamental basic of PCF and their sections are also briefly discussed. A detailed overview of the PCF structure implementation is given. Lastly, PCF based SPR sensors are reviewed critically in the last section.

### **2.2 Surface Plasmon and Surface Plasmon Resonance**

#### **2.2.1 Surface plasmon**

Surface Plasmons are coherent delocalized electron oscillation that exist at the interface between any two materials, Where the permittivity of one material is negative other is positive. Hence, the total density of charge in the conductor is zero. Surface plasmons travels at the interface of two medium and decays in both direction perpendicular to the interface. In the figure shown the wave travels in X direction and the decays travels in Z direction. This moving process will induce a longitudinal oscillation in the conductor and this is known as plasma oscillation known as surface plasmon[20].

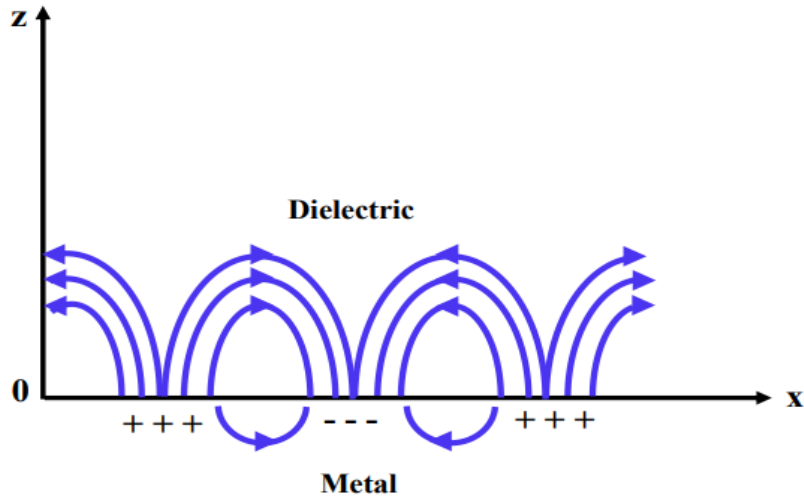


**Fig 2.1:** Plasmon oscillation in the metal [21].

### 2.2.2 Surface Plasmon Resonance

The phenomenon of surface plasmon resonance (SPR) occurs when incoming light photons at a certain angle of incidence excite electrons in the metal surface layer, which subsequently travel parallel to the metal surface[22]. The angle at which SPR occurs at thin metal surfaces is determined by the refractive index of the substance immediately next to the surface. Since SPR may be avoided by slightly altering the reflecting index of the sensing medium, this opens the door to sensitive analyte detection. The basic principle of SPR is based on incoming p-polarized light or transverse magnetic (TM) light of a certain frequency and plasmonic materials. When the surface electron are coincide, free electrons at the surface will fluctuate. For the oscillation of electrons, The Surface Plasmon Wave (SPW) is initiative with metal-dielectric interface which spread towards the surface. SPRW can be calculated by this equation[23],

$$\beta = \frac{\omega}{c} \sqrt{\frac{\epsilon^M \epsilon^D}{\epsilon^M + \epsilon^D}} \quad 2.1$$

Where  $\omega$  is the angular frequency,  $c$  is the speed of light,  $\epsilon^M$  defines dielectric permittivity's of metal and  $\epsilon^D$  is the dielectric surface. According to the above equation, the characteristics of SPW is entirely dependent on the two material which are metal and dielectric media.



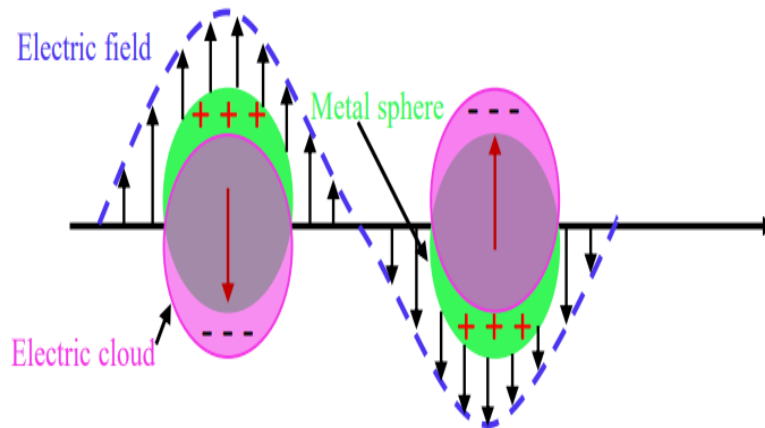


**Fig 2.2:** Localized SPR when field (light) interacts with the plasmons [24].

## 2.3 Surface plasmon resonance sensing technique

### 2.3.1 conventional Prism based SPR Configuration

Prism-based Conventional SPR sensor used to concentrate the incident light. When TM light or P polarized are strikes on a prism-metal dielectric interface, The reflection is measured as a function of angle of incidence. However, there is a sharp dip at a fixed angle of incident light called the resonance angle. The angular interrogation method is used to detect unknow analyte by measuring the shift of resonance wavelength. Based on the angular mechanism, auto-configuration and Kretschmann-configuration sensing techniques have been developed.

#### 2.3.1.1 Otto-configuration for SPR sensing

Otto-configuration sensing technique are developed in 1968, which involved placing a prism and metal in a gap and then filling the gap with the sample liquid [25]. The attenuated total reflection (ATR) technique is used in an Otto configuration. The evanescent wave (EW) is generated when light with p-polarization strikes the prism-dielectric interface, and at a certain angle, the evanescent wave excites the surface plasmon wave at the metal-dielectric interface.

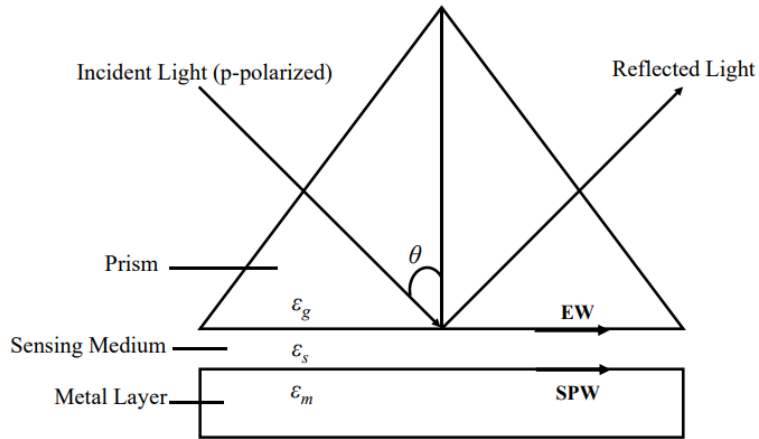


**Fig 2.3:** Otto-configuration for SPR sensor[26].

When the wave-vectors of an evanescent wave and a surface plasmon wave are aligned, a decrease in the intensity of the reflected wave is seen at that angle. In this state, the EW is able to transmit energy to the SPW. Here we calculate the evanescent field's wave vector  $k_{ev}$  at the prism-dielectric contact, where it is:

$$k_{ev} = \frac{\omega}{c} \sqrt{\epsilon_g} \sin \theta \dots\dots\dots 2.2$$

Where  $\omega$  denotes the frequency of incident light,  $C$  denotes the speed of light,  $\epsilon_g$  denotes the dielectric constant of the material of the prism and the incident angle is  $\theta$ .

The Otto-configuration has been useful for investigating the absorption properties of single crystal metal surfaces. One disadvantage of the Otto configuration is that it requires the prism and metal layer to be positioned with a limited spacing for the coupling to be effective. Through the process of resolving this issue, a new configuration (dubbed the Kretschmann configuration) is introduced.

**2.3.1.2 Kretschmann-configuration for SPR sensing**

Kretschmann-configuration for SPR sensing technique are introduced in 1968 where the prism and metal layer is attached together between the prism and metal layer there was no gap; sample liquids were placed outside the metal layer[27]. For this reason surface plasmon excited by the evanescent field wave as like as Otto- configuration. When the wave vectors of the surface plasmon wave and the evanescent wave coincided at a certain angle, resonance was produced.

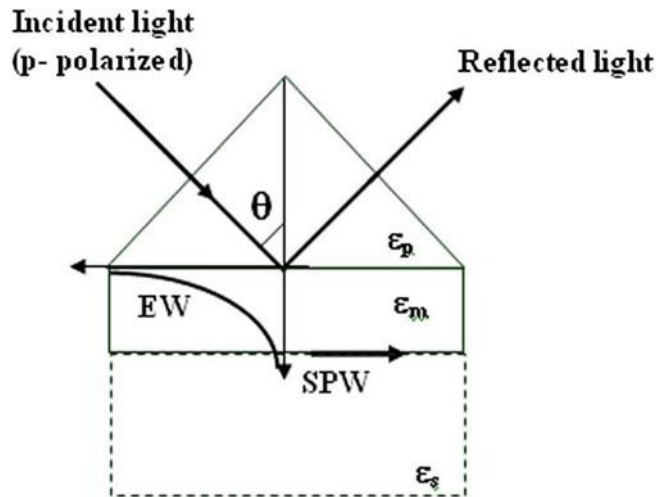


**Fig 2.4:** Kretschmann configuration for SPR sensor [28].

Under these resonance conditions, a drop in the intensity of the reflected light also developed. The incident light wave vector,  $k_g$  is defined as the wave vector of light traveling down the prism's surface, while the evanescent field wave vector,  $k_{ev}$  is described as,

$$k_{ev} = k_g \sin \theta = \frac{\omega}{c} \sqrt{\epsilon_g} \sin \theta \dots\dots\dots 2.3$$

The fundamental limitation of the Kretschmann-configuration is that the metal layer must be parallel to the prism surface, making it inapplicable to curved surfaces like a metal cylinder or a metal sphere. This is a contributing factor to the configuration's lack of widespread adoption [29].

### 2.3.2 Photonic crystal fiber surface plasmon resonance

The advancement of PCF and plasma science have been combined to create the PCF-based SPR sensor [14]. Photonic crystal fiber is a novel kind of optical fiber (PCF). Like typical optical fiber, it has a core and cladding, but in PCF, the cladding portion is made up of periodic air holes that can control how light is distributed. PCFs are also known as micro-structured optical fibers (MOFs) or holey fibers (HFs) [30]. It was not possible to combine the photonic crystal fiber-dependent SPR sensor with the conventional fiber optic SPR concept first. The PCF-sensing SPR's theory is particular to the kinds of structures. The modified total internal reflection (M-TIR) or photonic band gap (PBG) effects govern how light travels through PCFs [31]. Overall, light spreads wider through the middle of the fiber and many of the fields. Surface plasmon waves are generated when ephemeral plasmon fields interact with free electrons in the

metal layer and then propagate along the metal-dielectric contact. Up to a certain refractive index, the core-guided mode and the SPP mode are coupled at the same wavelength. This wavelength corresponds to a severe loss point for both the core-guided mode (actual value) and the SPP mode [10]. Phase-matching resonance disorder is another name for this condition. In order to function, the SPR sensor needs a metal component with a high number of unpaired electrons. The negative permittivity needed for plasmonic materials comes from such free electrons.

## **2.4 Fiber Optic Technology**

### **2.4.1 Conventional optical fiber**

Fiber optics, often known as optical fibers are frequently used in transmission of data or the directional guiding of light.[32] Each optical fiber has three parts: a core, a cladding, and a coating or buffer. The center portion of the optical fibers is called core which is made of glass and it is covered by a layer called cladding[33]. The core is a dielectric barrel-shaped pole. In terms of their structure, a refractive index of the core is greater while the cladding has a lower refractive index. which keeps light ray always within the core of optical fibers[33]. During the manufacturing of the optical fibers, protective layers of plastic are uniformly applied to the entire length of the fiber. The refractive index of the coating is higher than that of the cladding and core, to attenuate any undesirable light in the cladding[34]. This coating can be removed when desired, The coating gives protection to the fibers from external influences and absorbs shear forces. These coatings are usually colored to identify individual fibers in a multi-fibers cable[35]. The physical structure of a current optical fiber is seen in Fig:2.5. As a result, the optical fiber may be classified into two broad categories: single mode and multimode. Single-mode optical fibers have a particularly narrow core diameter (typically 9  $\mu\text{m}$ ), which restricts the transmission of light to a single wavelength[35]. Therefore, the attenuation is much reduced due to the lack of light leakage, and the signal may travel great distances. Single-mode fiber is commonly utilized by telecommunications companies, cable TV providers, and government agencies for runs longer than a few hundred meters. In contrast, multimode optical fibers have a larger core diameter (often 50  $\mu\text{m}$  or 62.5  $\mu\text{m}$ ) that allows for the propagation of many modes of light [36]. Data transmission rates are improved because of the larger amount of light that may flow through the center at any given time.

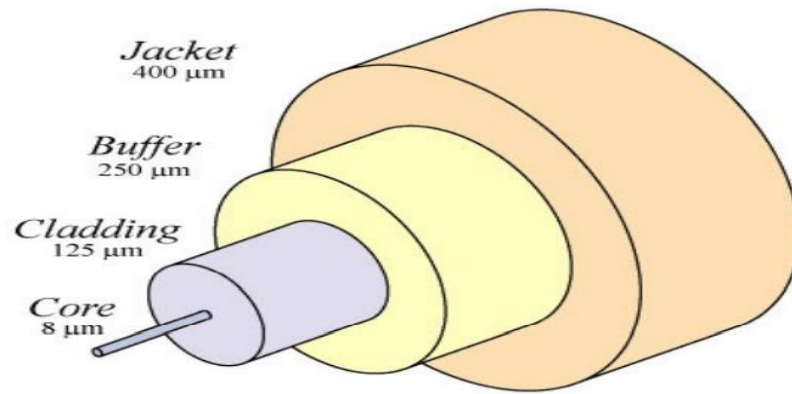


**Fig 2.5:** Conventional Optical fiber structure[36]

Multimode fibers are often utilized for short-range applications within data centers, LANs, and similar networks because to the dramatic loss in signal strength over longer distances caused by increased dispersion and attenuation levels[37]. Multimode fibers may be broken down into two basic styles.

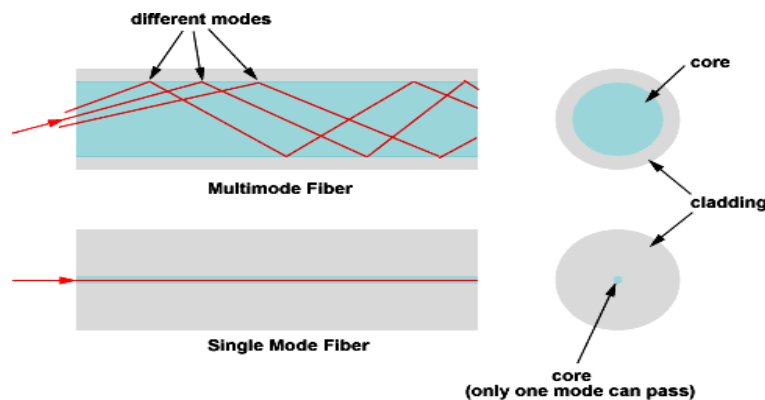


**Fig 2.6:** Multimode and Single-mode optical fiber[38].

## 2.4.2 Photonic crystal fiber

Since the mid-1990s, photonic crystal fibers (PCFs), also known as micro structured optical fibers (MOFs) or holey fibers (HFs), have been the focus of extensive research and have significantly impacted traditional fiber optics[39]. The PCF is a single optical fiber material made up of tiny air channels that run the length of the fiber. In order to make a low index cladding, air-holes are drilled into a silica basis, and the center is commonly made by either removing the central air-hole from the foundation or drilling a bigger air-hole in its place[40]. Cross sections of PCFs are typically either air-silica cladding around a robust silica core or air-silica cladding around a hollow core, as seen in Figur2.7. The guiding effects of total internal reflection (index guides) and photonic band gaps (PBG index guides) are maintained while

light travels through PCFs [41]. The PCFs' guiding process and modal features are distinct according to the air-holes' configuration, which includes the air-holes' number, size, form, and division. This endows PCF with a host of distinctive properties, such as single-mode operating throughout a broad wavelength range, a massive mode area, and atypical dispersion.

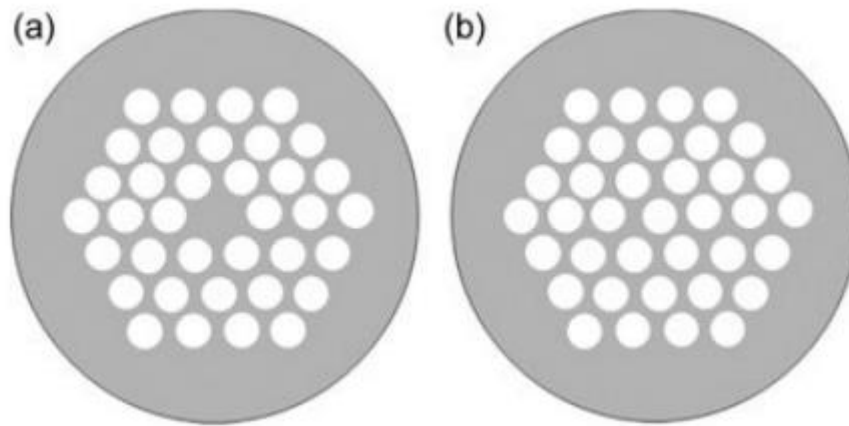


**Fig 2.7:** (a) Hollow core fiber cross-section (b) Solid core fiber cross-section [42]

## 2.5 PCF Structure Implementation

### 2.5.1 Geometrical definition

Based on the angular arrangement of air holes, PCF structures may be hexagonal, square, octagonal, decagonal, or a hybrid. In addition, as shown in Fig. 2.8, the apex angle of a triangle in a PCF with a hexagonal structure will be 60 degrees, whereas those of a PCF with an octagonal or decagonal structure will be 45 degrees and 30 degrees, respectively. Furthermore, the PCF's air holes are arranged in a periodic pattern, where  $d$  is the hole's diameter. The distance between any two consecutive airholes is called the pitch, and it is denoted by  $A$ .

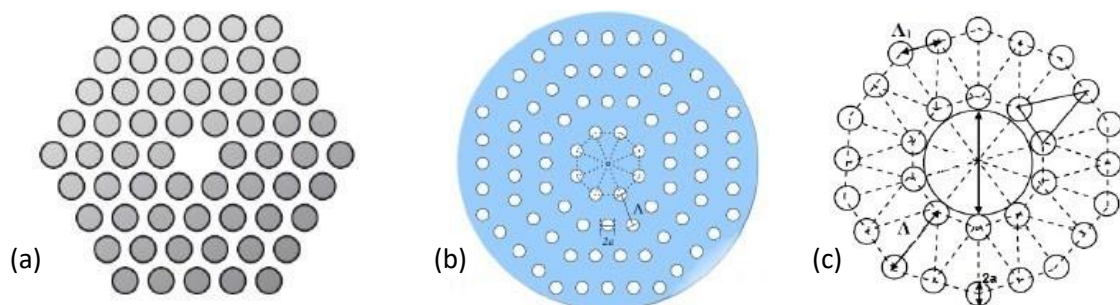


**Fig 2.8:** (a) Cross-section of hexagonal ( $60^{\circ}$  angle) PCF, (b) Cross-section view of octagonal ( $45^{\circ}$  angle) PCF, (c) cross-section view of decagonal ( $36^{\circ}$  angle) PCF.

## 2.5.2 Background material

The next phase, following the PCF's design, is to determine what parts will build up the final model. Both the core and the cladding of the fiber are typically made of fused silica (SiO<sub>2</sub>). Air holes with a refractive index of 1 may be found in the cladding region (around the core). According to the Sellmeier equation, we can characterize the distribution of the refractive index in silica[43].

$$n^2(\lambda) = 1 + \frac{B_1\lambda^2}{\lambda^2 - c_1} + \frac{B_2\lambda^2}{\lambda^2 - c_2} + \frac{B_3\lambda^2}{\lambda^2 - c_3} \dots\dots\dots 2.4$$

where n denotes the dependent on wavelength refractive index of fused silica (in m). In the Sellmeier equation, the constants B1, B2, B3, C1, C2, and C3 are as follows:

$$B1=0.69616300, \quad B2=0.407942600, \quad B3=0.897479400, \quad C1=0.00467914826, \\ C2=0.0135120631, \quad C3=97.9340025.$$

## 2.6 Performance Analysis Parameters

**Confinement Loss:** The confinement loss is used to explore all performance boundaries. From the imaginary component of the real effective index, the confinement loss may be calculated. Leakage of modes is equated with a loss of confinement. Although the core and cladding of PCF have the same effective refractive index (n<sub>a</sub>=1.44), the cladding is made up of air holes with a distinct refractive index (n<sub>a</sub>=1). Because of the limited number of air holes in the cladding, PCF guiding modes are inherently inefficient. If the cladding is made up of an unlimited number of air-holes, then PCFs will not experience any confinement losses. To put it theoretically, PCFs suffer from confinement losses due to the fact that their cladding is necessarily limited in size. Confinement losses can't affect a fiber with an infinite cladding. The core diameter, air-hole lattice, pitch, and ring count all play significant roles in the confinement loss. We may calculate the confinement loss at a given wavelength[44];

$$a(dB / cm) = 8686 \times \frac{2\pi}{\lambda} \times \text{Im}(n_{eff}) \times 10^4 \dots\dots\dots 2.5$$

where λ represents the active wavelength and Im(n<sub>eff</sub>) represents the imaginary component of the core mode's refractive index. Having a large confinement loss is bad for a sensor. Changes to the PCF structural parameters and the amount of air hole rings in the cladding area may be

used to fine-tune the confinement. Reduced confinement loss is achieved by the use of air hole rings to focus the core light inside the core.

**Wavelength Sensitivity:** Using wavelength interrogation, we can determine how sensitive a PCF-based SPR sensor is to certain wavelengths. To determine the wavelength sensitivity, use the following equation (Rifat et al., 2018):

$$S_{\lambda}(nm / RIU) = \Delta\lambda_{peak} / \Delta na \dots\dots\dots 2.6$$

where  $\Delta\lambda$  represents the dispersion of the resonant wavelength and  $\Delta na$  represents the RI shift due to the analyte. However, the detection approach is complicated since the wavelength interrogation method manipulates the spectrum to acquire the sensitivity.

**Amplitude Sensitivity:** Amplitude sensitivity is an alternative method for evaluating sensor efficiency. In contrast to getting the wavelength sensitivity, which requires spectral manipulation, the amplitude sensitivity may be obtained using the amplitude interrogation technique, which is both straightforward and cost-effective. Here is an equation for determining amplitude sensitivity [46].

$$S_A = -\frac{1}{\alpha(\lambda, n_a)} \frac{\partial \alpha(\lambda n_a)}{\partial n_a} \dots\dots\dots 2.7$$

where  $\alpha(\lambda n_a)$  represents the loss in transmission at any wavelength and  $\partial \alpha(\lambda n_a)$  represents the difference in propagation loss between two spectral losses.

**Sensor Resolution:** The resolution of the sensor is another performance sensing metric that reveals the sensor's sensitivity to detect changes in the RI of the analyte. Sensor resolution is proportional to the sensor's wavelength sensitivity. Resolution is determined by the following equation[47].

$$R(RIU) = \Delta na \times \Delta\lambda_{min} / \Delta\lambda_{peak} \dots\dots\dots 2.8$$

where  $\Delta na$  represents the variation in RI of the analytes,  $\Delta\lambda_{min}$  specifies the lowest possible spectral resolution, and  $\lambda_{peak}$  denotes the largest possible variation in the resonant wavelength. For example, if  $\Delta na = 0.01$ ,  $\Delta\lambda_{min} = 0.1$ , and  $\Delta\lambda_{peak} = 100$  nm, then the sensor resolution is predicted to be 1105 RIU, indicating that it can detect a 105 RIU difference in the RI of the analyte.

**Figure of Merit (FOM):** Basically, figure of merit is a metric that measures how well a sensor performs. The FOM is determined using the sensor's FWHM, or full width at half maximum.



As the analyte RI rises, the loss spectrum widens, causing the FWHM value to drop. The sensitivity of a sensor is also a factor in determining how much FOM is worth. However, using the following equation FOM may be calculated[48]:

$$FOM = \frac{S(\frac{nm}{RIU})}{FWHM(nm)} \dots\dots\dots 2.9$$

where S represents the wavelength interrogation sensitivity and FWHM the full width at half maximum.

**Birefringence:** A sensor's polarization dependence is described by its birefringence features. Depending on its construction, a sensor may exhibit sensing response in either a single- or dual-polarization mode. For a complete definition of birefringence (B) qualities, we may use the equation[49],

$$B = | n_x - n_y | \dots\dots\dots 2.10$$

where  $n_x$  and  $n_y$  stand for the real refractive indices of the x and y polarized modes, respectively. For a given magnitude of the dissimilarity between the x and y polarized modes, the value of B will rise proportionally. This striking contrast suggests that the sensor is capable of high light coupling and substantial forward shifting of the resonant wavelength in a single polarization mode, which may be x or y polarization mode. If B is always the same or close to zero, then the sensor is polarization independent (it may be used for sensing in any polarization mode).

## 2.7 Literature Review on PCF based SPR Sensors

The performance of SPR sensors has been significantly improved due to a number of notable works published during the last few decades. Medical diagnostics, biomolecular detection, and antibody-antigen interaction are only few of the sensing areas where the PCF-based SPR sensor has excelled[45]. Initially, prisms were utilized for SPR sensors; however, PCF based SPR sensors began attracting more attention owing to their advantages (small size, distant sensing capability, etc.). In addition, the miniaturization of PCF-based SPR sensors facilitates their incorporation into existing systems[14]. For the first time in 2006, the idea of an SPR sensor based on a MOF was offered. This sensor would have a PCF structure consisting of two concentric rings[50]. To facilitate the flow of the analyte, (Rifat et al.) presented a sensor with a gold coating on the inside and a wide air hole Figure 2.9 (a). The sensor has a maximum

sensitivity of 11,000 nm/RIU (wavelength) and 1420 RIU-1 (amplitude) in the 1.33-1.42 analyte detection range[10]. By coating the analyte channels with gold and titanium dioxide (TiO<sub>2</sub>),[51] presented a single hexagonal layer-based SPR sensor Figure 2.14 (b). Maximum sensitivity is 370 RIU-1 and resolution is  $2.70 \times 10^5$  RIU. Qin et al. presented a polymer PCF-based SPR biosensor with a reported wavelength sensitivity of 4354.3 nm/RIU.

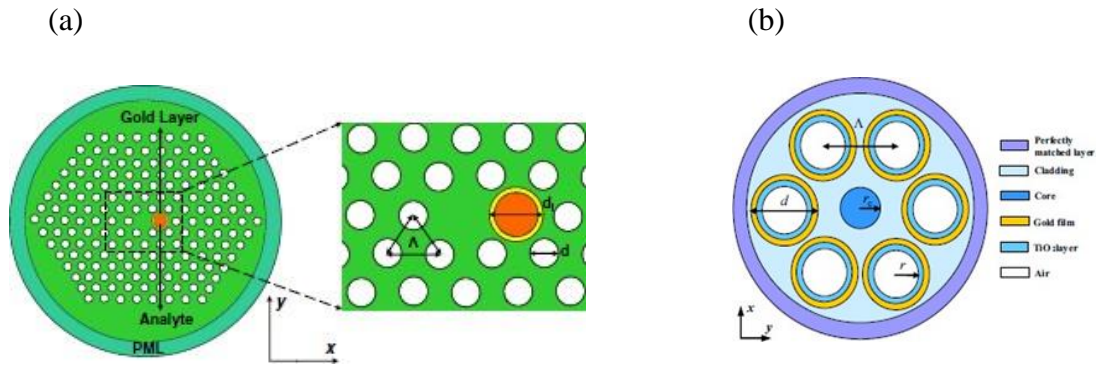


**Fig 2.9:** (a) & (b) Cross-section view of the sensor and selective air hole metal coating[10][51].

A second PCF is presented with the same basic arrangement, but this time the sensitivity is increased by using a graphene-silver bimetallic layer, resulting in a maximum sensitivity of 2520 nm/RIU and a resolution of  $3.97 \times 10^{-5}$  RIU [52]. Kaur et al. have recently published a multichannel PCF based SPR sensor with two sensing layers. The two gold-coated layers have a maximum sensitivity of 1000 nm/RIU and 3750 nm/RIU to light at those wavelengths [53]. In their study, Guowen et al. looked at an ultra-wide PCF sensor with a covering made of a triangular lattice and four large-size air holes serving as analyte channels[54]. The suggested sensor has an analyte RI sensing range of 1.30-1.79. Filling the inner air-holes with analyte and selectively metal-coating the air-holes are, nevertheless, difficult and labor-intensive processes. A PCF sensor in the form of a letter "D" is the answer to this predicament.

Many researches have shown that D-shaped PCF-based SPR sensors perform well in terms of detecting range, wavelength, and amplitude sensitivity[55]. D-shaped sensors are challenging to make due to the exact polishing necessary for the liquid channel layer. Many researches have shown that D-shaped PCF-based SPR sensors perform well in terms of detecting range, wavelength, and amplitude sensitivity[56]. D-shaped sensors are challenging to make due to the exact polishing necessary for the liquid channel layer.

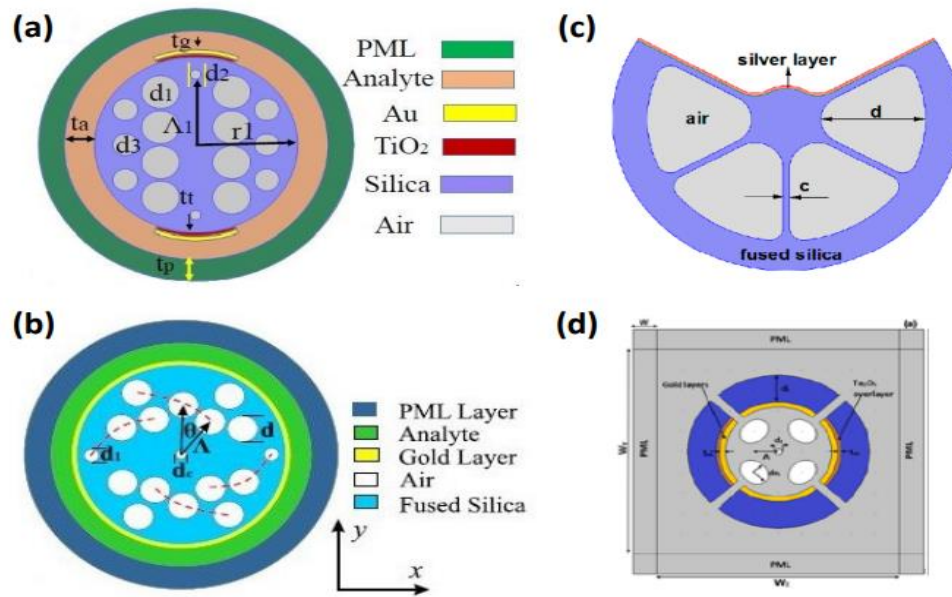


**Fig 2.10:** Cross section view of external sensing approach (a) Rectangular core-based PCF sensor (Islam et al., 2019b), (b) spiral PCF sensor[46] (c) Schematic of the designed exposed-core grapefruit fiber based SPR sensor [20], (d) microfluidic slotted based sensor for multi-analytes detection[57].

Graphene, a man-made 2D nanomaterial that has attracted a lot of interest since its creation over a decade ago, is particularly useful for SPR-based sensors due to its exceptional capacity to absorb biomolecules[58]. Graphene is a kind of carbon that is so thin that just one atom can be seen through it. Atoms are arranged in such a way that they form a honeycomb-like hexagonal lattice[59]. It demonstrates strong optical conductivity from near to mid-infrared (NMR) frequency due of its inter-band transition. It has a significant surface-to-volume ratio which facilitates good biocompatibility. It also exhibits good compatibility with active metals (Au, Ag, and Cu) due to its rich  $\pi$ - $\pi$  stacking which enhances the sensitivity of SPR-based sensors[60]. Recently, various graphene-based sensors have been proposed. Among them, Song et al. (2010) reported the fabricated work in which a thin sheet of graphene is coated on Au to make it a substrate material. It is used as a biomolecular recognition element (BRE) for the functionalization of the gold surface so that the biomolecule adsorption can be increased on the gold surface[61]. Although graphene is extensively used as a 2D material but apart from that, another 2D material exists such as MoS2 which belongs to transition metal dichalcogenides (TMDs)[62]. It brings out much attention because of its better optical absorption and band gap tunability which is also comparable with graphene.

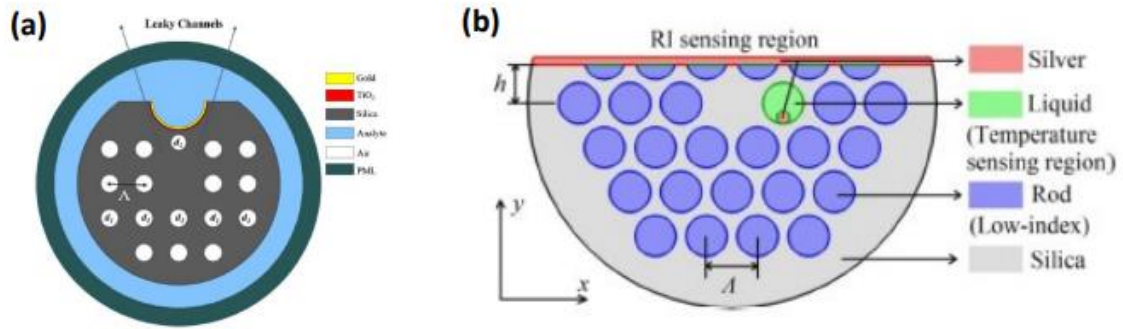


**Fig 2.11:** (a) A microchannel based D-shaped PCF sensor[48] (b) D-type PCF based SPR sensor for sensing analyte RI and temperature [63])

Currently, most SPR-based sensors use an external sensing method in which the analyte is directly deposited on a grease-polished surface. This method improves real-time sensing because it eliminates the covering or filling of air pores[64]. The D-shaped PCF structure is useful for external sensing. Recently, several D-shaped sensors have been reported. Among these, a D-shaped optical sensor is described by[65]. The flat layer on top of the PCF is coated with gold. SPR effects were observed between the basic mode and SPP modes, allowing one to track changes in the analyte's RI. Therefore, for RI values ranging from 1.43 to 1.46, we were able to determine an average wavelength sensitivity of 7700 nm/RIU and a resolution of  $1.30 \times 10^5$  RIU[66]. To test the PCF's sensing capabilities, the researchers varied the thickness of the gold coating. With a sensitive resolution of  $9.53 \times 10^6$  RIU, it was determined that the best sensitivity was obtained for the RI value range of 1.33 to 1.38, where the sensitivity plateaued. For their RI sensor proposal a D-shaped PCF with a fatty, side-polished part as the active area and coated it with a gold coating. Sensing performance is improved by adjusting the thickness of the gold layer and the diameter of the largest air hole. After modeling, the highest achievable sensitivity was 31,000 nm/RIU, giving an effective sensor resolution of  $3.31 \times 10^5$  RIU. Also, the use of sonar causes a significant wavelength shift in the resonance frequency, which improves analyte detection.

## **CHAPTER 3: METHODOLOGY**

### **3.1 Introduction**

In this chapter, the design of the proposed PCF-based SPR double side D shape sensor design is explained in detail. This chapter also includes a description of the numerical characterization of the proposed model and the optimization method.

### **3.2 Design Structure**

We present a D-shaped planar carbon fiber (PCF) based SPR sensor with high sensitivity and low polishing effort. The majority of the reported D-shaped PCF-based SPR sensors are built on a foundation of intensive polishing. However, the fiber's fragility makes it difficult to achieve a high polishing depth in the production process. Therefore, a microchannel was added as a liquid channel into the suggested design to enhance the contact between the core and the metal surface. This helps by decreasing the polishing depth, increasing the light coupling intensity, and decreasing the likelihood of fiber break. Figure 3.1(a) is a cross-sectional 2D view of the proposed PCF sensor. The fundamental issue with the design in Fig 3.1(a) is the complexity of manufacturing that results from the need to create a microchannel with such a square lattice air - holes arrangement.

Therefore, the airholes was adopted to construct the proposed double-side D-shaped PCF-based SPR sensor for a better light-guiding mechanism via core and cladding. Fibers may be manufactured using the stack-and-draw fiber drawing process. This process is easy to use and very efficient for creating long-length fibers, unlike other fiber fabrication strategies including extrusion, sol-gel casting, injection molding, and drilling. In Figure 3.1(a), we see a cross-section of the planned sensor's microchannels, which are covered with plasmonic metals.

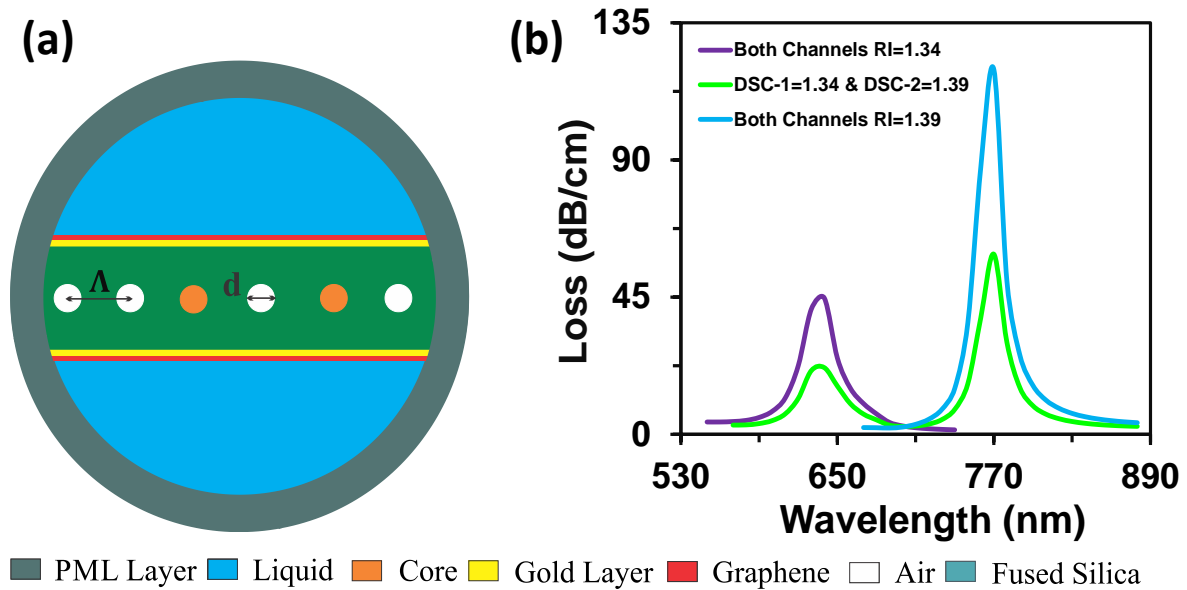


**Fig 3.1:** (a) a cross-sectional 2D view of the PCF sensor. (b) Verification of multianalyte operation feasibility.

We have finalized the optimum value for regular air hole diameter ( $d$ ) which is  $1.95 \mu\text{m}$ . The proposed PCF consists of constant center-to-center spacing (pitch size,  $\Lambda$ ) of two air holes located next to each other. After validating the pure fiber for several pitches, we selected the optimum pitch to be  $2.028 \mu\text{m}$ . In terms of performance, we showed that an Au nanolayer with a width ( $t$ ) of  $35 \text{ nm}$  exhibited improved sensitivity. We used graphene layer nanoparticle deposition upon the Au layer because the Au coating is adhered to the silica using a thin adhesive layer of graphene.

After choosing the materials from the COMSOL library, the optical parameter complex refractive index must be entered by hand. The correct material has been inserted, the whole electric field has been laid out using the Electromagnetic Waves Frequency Domain (ewfd) physic interface, and the electric field displacement model has been selected as the refractive index model.

### 3.3 Boundary setting

Determining boundaries is a major challenge in numerical simulations. Propagation loss is critical to the performance of an SPR sensor implemented in PCF. The imaginary part of the effective refractive index, the  $\text{Im}[n_{\text{eff}}]$  value, is used to determine propagation loss. As the light that passes, part of it is dispersed and reflected by the surface, which dampens the effect. As a result, PML boundary conditions are often utilized to minimize surface reflections when

light is emitted toward the boundary and absorbed at the surface. As a result, the reflected light is absorbed by the PML layer to prevent the false-positive response (Fig 3.2).

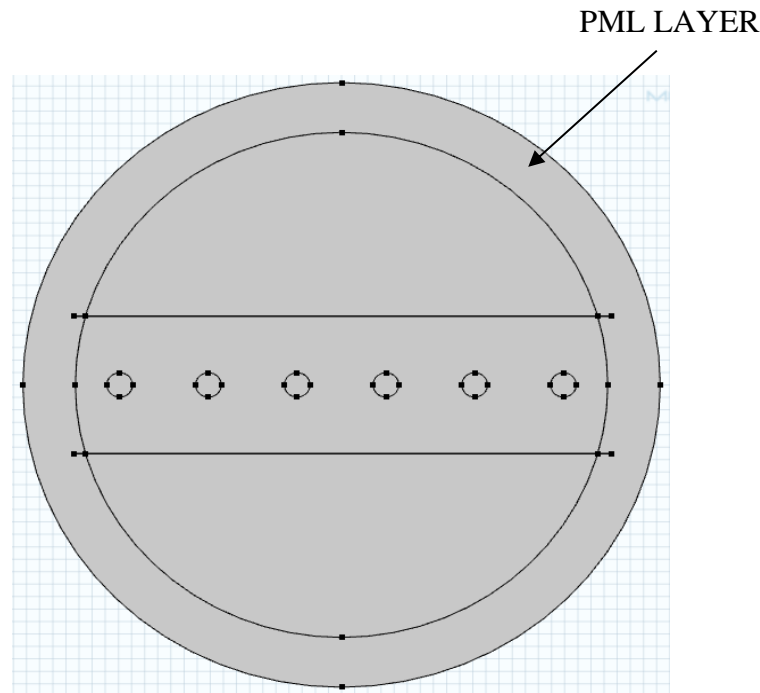


**Fig 3.2:** PML boundary layer

### 3.4 Meshing

The area of computation may be divided into a limited number of tiny triangular or rectangular sections known as mesh. In order to assess the robustness of a system, meshing is a crucial factor. Widening the mesh in the numerical region where light travels allow for a more precise examination of the distribution. For each mesh type, the number of mesh components is indicated by the mesh size. Increasing the mesh's element count helps the numerical simulation immensely. This implies the statistical region may be narrowed down to a more manageable size, increasing the test's potential for accuracy. Meshes are seen in Fig 3.3

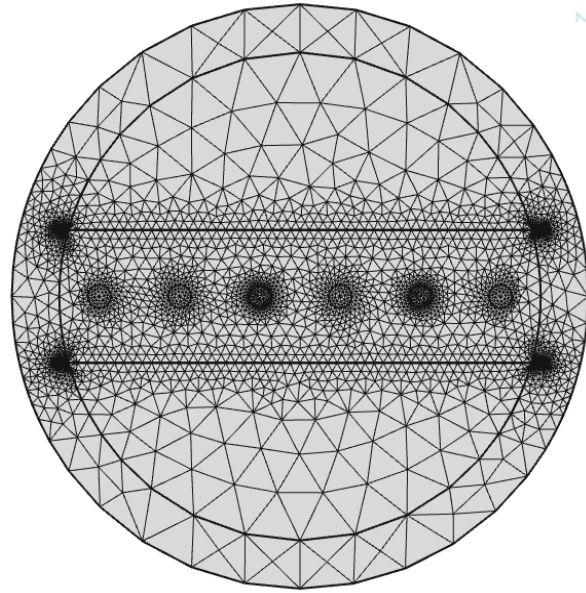


**Fig 3.3:** Mesh

### **3.5 Plasmonic Materials for the Proposed Sensor**

The sensitivity of a PCF-based SPR sensor may be improved by the addition of plasmonic metal. When it comes to SPR sensors, a plasmonic substance is required because of its ability to release many electrons. The fundamental structural component of the suggested D-shaped sensor is fused silica ( $\text{SiO}_2$ ). High mechanical strength against pulling, a broad wavelength range, low absorption, and low dispersion are all characteristics of fused silica. Equation 2.8 is used to describe the silica's refractive index. Also, gold (Au) is used mostly as a plasmonic material because of its chemical stability and shows large resonance peak shift. However, the dielectric constant of gold can be evaluated using Equation 2.9. In practice, the gold layer cannot attach properly on the silica. So, graphene is used as an adhesive layer, which causes a greater forward shift in the resonance wavelength. A major difficulty during fabrication is pinpointing exactly where on the PCF surface the Au layer should be applied. It is common practice to deposit the gold layer through chemical vapor deposition[67]. In addition, a novel ALD technique has recently been revealed that precisely coats a tiny gold layer in a curved surface.



### 3.6 Research Model

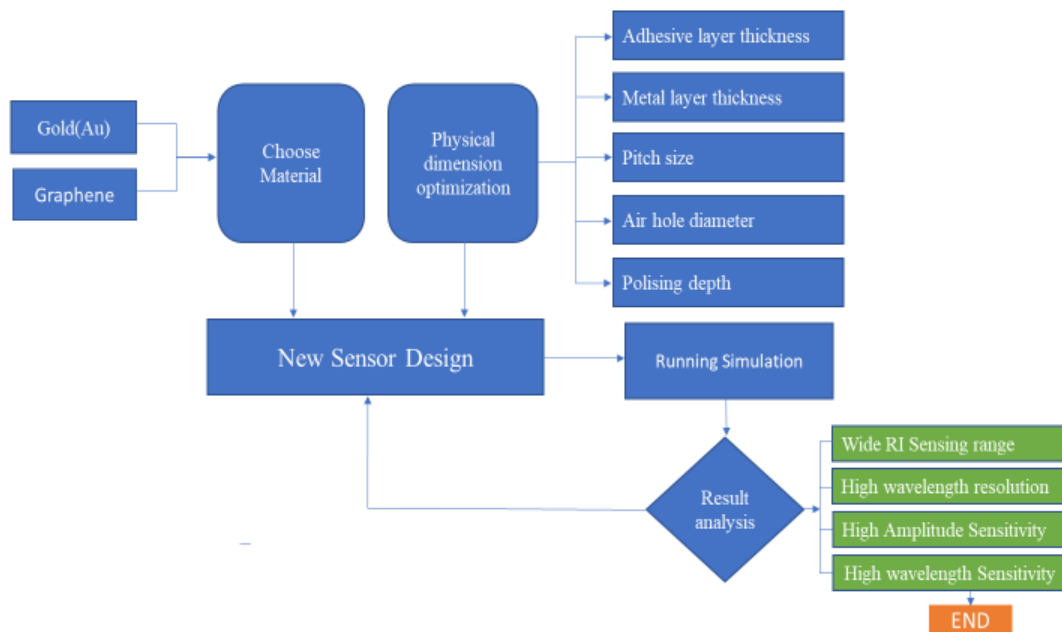


**Fig 3.4:** Basic simulation layout for the proposed sensor

A simplified workflow of the computational method used in this study is shown in Figure 3.2. The FEM is studied, calculated, and implemented in COMSOL Multiphysics. Initially, all the structural characteristics are used to create a D-shaped PCF sensor in COMSOL Multiphysics. Plasmonic material is used to create surface plasmon phenomena at the metal-dielectric contact (graphene, gold). After the design is finished, the sensor's structural properties are optimized so that it can work at its best. When all of the design parameters are optimized, the final design is produced. The computational analysis data are taken from COMSOL and entered into MATLAB to examine the sensor's sensing performance. A redesign of the design will be carried out if the sensor's performances are not adequate when compared to the literature evaluation. The procedure will thereafter come to an end if the findings are acceptable.

### 3.7 Numerical Tools

Due to a shortage of available experiments, simulation-based solutions have been developed for a wide range of difficult, real-world situations. Using simulation software, a close numerical solution may be found. Errors in the numerical solution in comparison to the experimental solution are tolerable but not to be ignored. In this case, numerical findings provide the basis

for the approximations. For numerical analysis, the finite element technique may be utilized with Maxwell's equations.

The COMSOL Multiphysics is a universal platform that can perform eigen-frequency and modal analysis. This software has several features include 2D and 3D AC/DC circuit modeling, acoustics, electrochemistry, fluid-flow, frequency-dependent equation solving, the finite element approach, multiphysics coupling, and more. COMSOL Multi-physics version 5.4 is used to design the suggested D-shaped PCF structure. since it allows for the definition of boundary conditions and sub-domains with the appropriate parameters for resolving electric and magnetic field issues. Version R2016a of MATLAB® is a high-level programming language and interactive environment for visualization and numerical calculation. Its capacity for numerical calculation has been used to evaluate performance metrics such as interrogation modes, birefringence, and confinement loss. As compared to conventional programming languages, the tools and built-in math functions provide numerous ways to arrive at a solution more quickly.

## CHAPTER 4: RESULT AND DISCUSSION

### 4.1 Introduction

The PCF-based SPR sensor's detection process is wholly dependent on fiber-based light-guiding phenomena. The maximal SPP excitation at the metal-analyte interface for a certain wavelength, known as the resonant wavelength, is spontaneously endorsed by the penetrated evanescent field when the resonance condition is fulfilled. As a result, a strong confinement loss spectrum emerges and changes in response to analyte RI fluctuation. This occurs as a result of the core and plasmon modes' true effective mode indices crossing at that same optical frequency.

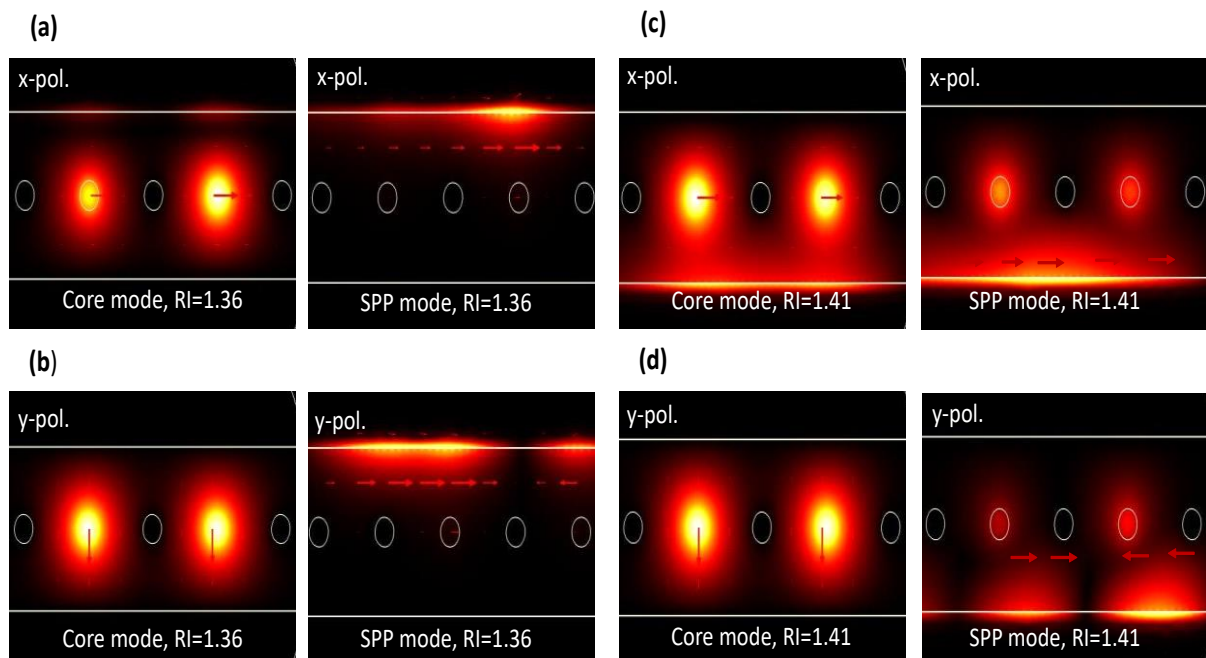


**Fig 4.1:** Distribution of electric fields for core-guided mode and SPP mode (a & c) at analyte RI 1.36 for channel 1 and (c & d) at analyte RI 1.41 for channel 2.

### 4.2 Multi-analyte Sensing

Figure 4.1 shows that the x-polarized mode has a stronger light coupling intensity than the y-polarized mode. Figures 4(a-c) and 4(b-d) show the electric field distributions of core-directed and SPP modes for RI of 1.36 and 1.42, respectively. Figure 4.2 (a) illustrates the matching phenomenon as well as the loss spectrum for channels 1 and channel 2 after they have been

infiltrated with analyte with RI values of 1.36 and 1.42. Maximum energy from core mode transmitted to SPP occurs at 616 nm and 870 nm for the corresponding RIs in x-polarized mode when the phase-matching phenomenon occurs. The core-guided mode is represented by real ( $n_{eff}$ ), while the SPP mode is represented by y-polarization, as shown in Fig. 4(a). The true ( $n_{eff}$ ) wavelength of the core-guided mode and the SPP mode intersect at 870 nm (when RI is 1.42) in the solid orange line and dashed orange line.

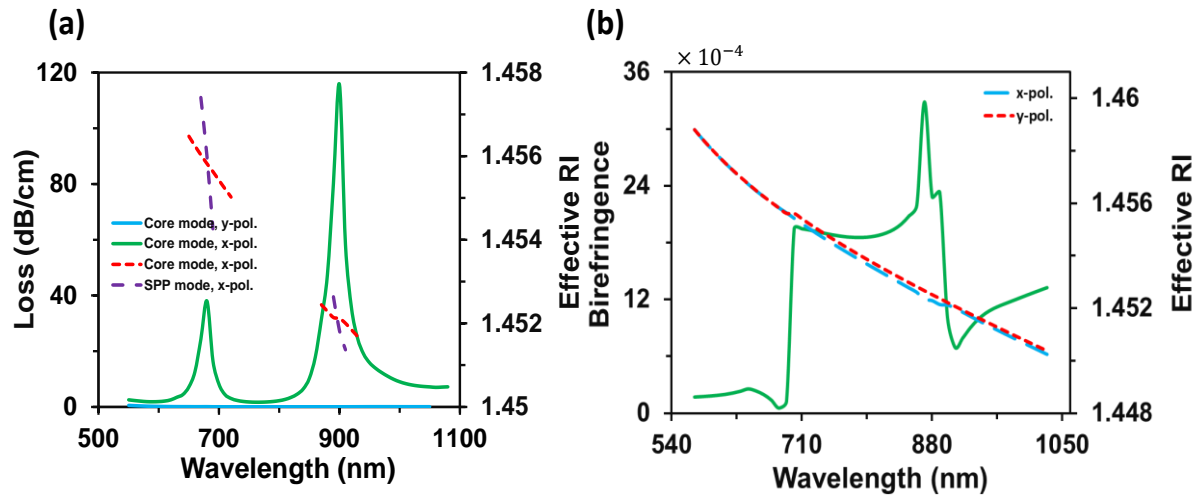


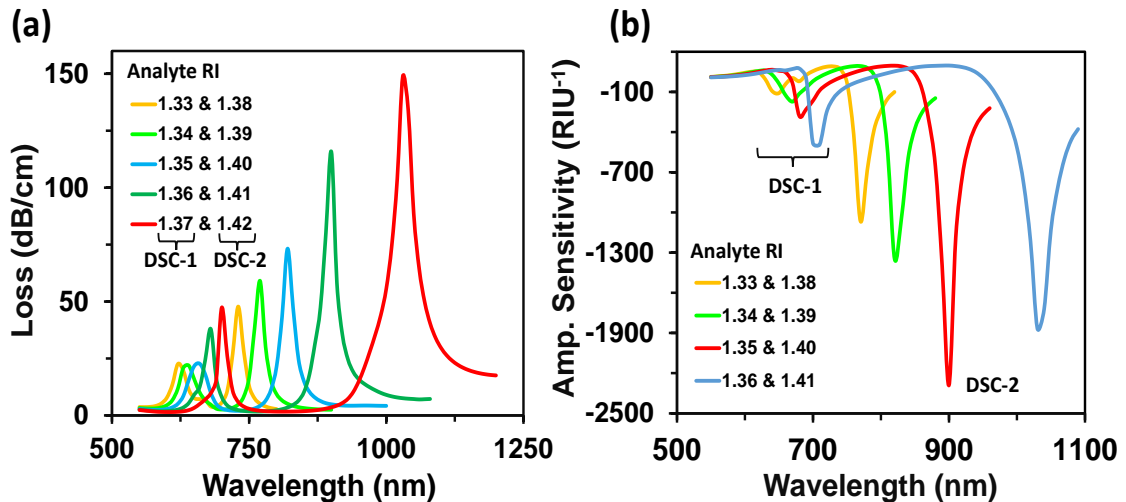
**Fig 4.2:** (a) Satisfied phase-matching condition for multi-Analyte detection. (b) Birefringence characteristics

However, the resonant wavelength for the analyte RI of 1.36 is 616 nm, where the orange dotted line and orange dashed line, representing the real( $n_{eff}$ ) of core-guided mode and SPP mode, meet. To demonstrate the proposed sensor's simultaneous multi-analyte detection capacity, we have selected two distinct RIs for sensing channels and provided phase-matching conditions in a single loss spectrum. In addition, the sensor shows stronger coupling and a sharper loss spectrum in x-polarization than in y-polarization (Figure 4.2 (a)). Therefore the sensor's efficacy was analyzed by focusing on the x-polarized mode, where coupling is very high. According to Fig. 4.2 (a), it appears that single SPP mode induced to couple with the core mode while the other one is left off for a certain RI (table in Fig4.2(a)) Because, depending on the sample RI at different spectral wavelengths, the core mode and the plasmon mode couple independently to the two liquid channels. This shows that channel 1 and channel 2 fluids are respectively responsible for the first and second peaks of the single loss spectrum. The confinement loss ( $\alpha$ ) at a specific wavelength is evaluated by 2.5. The functional wavelength is expressed in micrometers, and the value of  $\text{Im}(n_{eff})$  shows the imaginary component of the effective mode RI.

**Table 1. Performance information of the proposed multi-analyte operation**

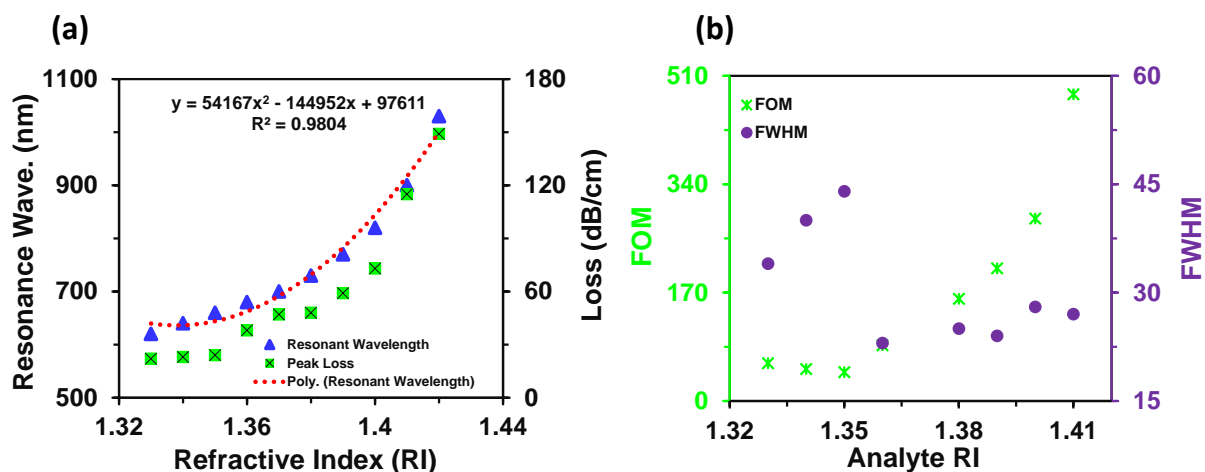
Channel	Analyte RI	Pol. mode	Peak Loss (dB/cm)	Res. Peak Wave. (nm)	Res. peak Shift (nm)	Wavelength sensitivity (nm/RIU)	Wavelength resolution (RIU)	Amp. sens. (RIU <sup>-1</sup> )	FWHM	FOM
DSC-1	1.33	x-pol.	22	620	20	2,000	$5 \times 10^{-5}$	109	34	59
	1.34	x-pol.	23	640	20	2,000	$5 \times 10^{-5}$	172	40	50
	1.35	x-pol.	24	660	20	2,000	$5 \times 10^{-5}$	280	44	45
	1.36	x-pol.	38	680	20	2,000	$5 \times 10^{-5}$	493	23	87
	1.37	x-pol.	47	700	N/A	N/A	N/A	N/A	19	N/A
DSC-2	1.38	x-pol.	48	730	40	4,000	$2.5 \times 10^{-5}$	1066	25	160
	1.39	x-pol.	59	770	50	5,000	$2.0 \times 10^{-5}$	1348	24	208
	1.40	x-pol.	73	820	80	8,000	$1.3 \times 10^{-5}$	2291	28	286
	1.41	x-pol.	115	900	130	13,000	$7.7 \times 10^{-6}$	1865	27	481
	1.42	x-pol.	149	1030	N/A	N/A	N/A	N/A	46	N/A

Fig. 4.2 (b) shows the structure's strong birefringence property for analytes with RIs of 1.36 and 1.42 when they are filled in various channels. The mathematical equation by 2.10 describes a structure's birefringence. It has been observed that the suggested sensor exhibits high birefringence around the resonant wavelength of RI 1.36 and RI 1.41, with values of  $3.3 \times 10^{-4}$  and  $1.3 \times 10^{-4}$ , respectively. This indicates the sensor has a strong polarization dependence and may operate in either the x- or y-polarization mode. In addition, when both channels are filled with low and high analyte RI [68], the propagating light causes the birefringence values to display an irregular spectrum (see Figure 4b). To confirm the viability of real-time operation, a spectrum study of multi-analyte sensing is conducted by concurrently altering analyte RI[69].



**Fig 4.3:** For multi-analyte detection, (a) right shift of SPR with any increase in RI of the infiltrated liquid, (b) amplitude sensitivities for different RIs.

Figure 4.3 (a) displays the loss spectra for paired analyte implantation. The full visible RI range (1.33-1.42) is separated into two groups, one for penetration in channel 1 and the other for penetration in channel 2. We chose lower RI samples between 1.33 and 1.37 for channel 1, and higher RI samples between 1.38 and 1.42 for channel 2. The analyte with RI 1.42 shows the largest energy transfer and strongest coupling in a multi-analyte operation, with a loss depth of 149 dB/cm. The lowest coupling occurs at analyte RI 1.33, where the modal loss is just 22 dB/cm at 620 nm. The most obvious wavelength difference is noticed between RI 1.41-1.42, which corresponds to 149 nm. This sensor has a maximum wavelength sensitivity of 13000 nm/RIU at RI 1.41. A sensor's sensitivity is determined by the tight coupling between the core guided mode and the SPP mode. The strong connection between the core-guided mode and the SPP mode is heavily dependent on the refractive index contrast between the fiber-core and the analyte RI[70]. The refractive index disparity between the core-guided mode and the SPP mode is considerable for lower analyte RI ( $n_a = 1.33$ ), and as a consequence, most of the light confines in the fiber-core. However, when analyte RI increases, the refractive index difference between the core mode and the SPP mode becomes extremely tiny. Because of this slight variation in RI contrast, the sensor has less light confinement in the core and more light coupling at the metal surface, resulting in larger confinement loss. The sensor becomes increasingly sensitive and displays a considerable resonant wavelength shift even for minor RI fluctuations due to strong coupling at increased analyte RI.



**Fig 4.4:** (a) Loss peaks and 2nd order polynomial fitting of the resonant wavelength with respect to RI, (b) the relation between FOM and FWHM at individual RI.

The magnitude of sensor resolution defines the smallest detectable change in RI and is evaluated by the equation as 2.8. We determined that the optimal sensor resolution is  $7.7 \times 10^{-6}$

RIU. Another cost-effective sensor performance metric is amplitude sensitivity, since spectral interpolation is unnecessary here. Fig. 4.3 b illustrates the amplitude sensitivities of all detected analytes, which are measured using the equation 2.5. The sensor has the lowest and maximum amplitude sensitivity for analyte RI values of 1.35 and 1.40, which approximate to about 109 and 2291 RIU-1, respectively. The fitting of a second-order polynomial curve is shown in Fig. 4.4 (a), where the R2 value was calculated to be 0.9804, which is exceptionally near to unity. This suggests that a fast-calculating method is sufficient for achieving high precision. Figure 4.4 (b) displays the figure of merit (FOM) and full width at half-maximum (FWHM) values for several analytes. The FOM indicates the output efficiency of the sensor and is defined as the ratio of wavelength sensitivity and respective FWHM. For this sensor, the FOM value may reach a maximum of 474 RIU-1 at its highest point.

**Table 2. Performance information of the proposed single analyte operation.**

Analyte RI	Polarization mode	Peak Loss (dB/cm)	Res.Peak Wave. (nm)	Res.peak Shift (nm)	Wavelength sensitivity (nm/RIU)	Wavelength resolution (RIU)	Amp. sens. (RIU <sup>-1</sup> )
1.33	x-pol.	42	620	20	2,000	5×10 <sup>-5</sup>	132
1.34	x-pol.	45	640	10	1,000	1×10 <sup>-4</sup>	204
1.35	x-pol.	48	650	30	3,000	3.3×10 <sup>-5</sup>	351
1.36	x-pol.	64	680	20	2,000	5×10 <sup>-5</sup>	501
1.37	x-pol.	87	700	30	3,000	3.3×10 <sup>-5</sup>	858
1.38	x-pol.	102	730	40	4,000	2.5×10 <sup>-5</sup>	1,296
1.39	x-pol.	120	770	50	5,000	2.0×10 <sup>-5</sup>	2,033
1.40	x-pol.	181	820	70	7,000	1.4×10 <sup>-5</sup>	2,063
1.41	x-pol.	190	890	130	13,000	7.7×10 <sup>-6</sup>	1,813
1.42	x-pol.	234	1020	N/A	N/A	N/A	N/A

### 4.3 Single-analyte sensing

Our proposed sensor can also detect a single analyte which reduce the chance of a false-positive result. The detection of a single analyte may be accomplished in one of two ways: either by infiltrating liquid sample (analyte RI) into just one channel and leaving the other channel empty, or by filling both channels with the same analyte RI.

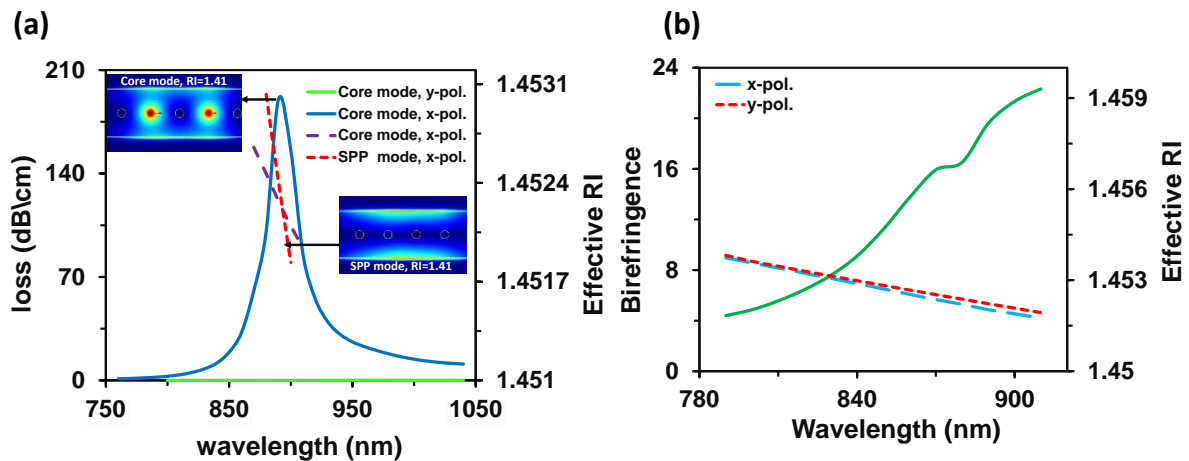


**Fig 4.5:** (a) phase matching at RI 1.41 (b) Birefringence character of the sensor.

Figure 4.5 displays the confinement loss curves and verifies the phase-matching requirement for x- and y-polarized light transmission when both channels are filled with RI 1.41 liquid. Fig 4.5 (a) demonstrates that the loss component of y-polarization is lower and flatter than that of x-polarization. Due to the less intense nature of this investigation, y-polarization analysis is omitted. Figure 4b illustrates the strong birefringence characteristic of the structure for analyte RI of 1.41 while using a single-analyte sensing (both channels were filled with the same analyte). For the proposed sensor, high birefringence of  $1.45 \times 10^{-4}$  is observed at the resonant wavelength of RI 1.41. In addition, birefringence values exhibit a regular spectrum (see Figure 4.5 (b)) as a result of real - time coupling of propagating light with both channels containing the same analyte RI. Figure 4.6 shows the loss spectrum for increasing the analyte RI from 1.33 to 1.42 in the single-analyte sensing system (both channels were filled with the same analyte) in comparison to the multi-analyte sensing system. Because the SPP mode turns on at the same frequency (both channels correspond to the same analyte RI) for both channels Fig. 4.6(a). In contrast to RI 1.42, which exhibits a maximum loss magnitude of 234 dB/cm at 1020 nm, the analyte RI 1.33 has a minimum loss depth of 42 dB/cm at 620 nm (see Table 2). Due to the fact that the wavelength sensitivities obtained are very stable (100 nm/RIU variation at most), and the spectral location of these peaks has not changed more than 2 nm (at worst) in the reverse direction from those of multi-analyte trials. Tables 1 and 2 may provide this statistic as well as additional comparable sensing information. The amplitude sensitivities of all analytes are shown in Fig. 8b, with the maximum amplitude sensitivity of 2063 RIU<sup>-1</sup> at RI 1.40.



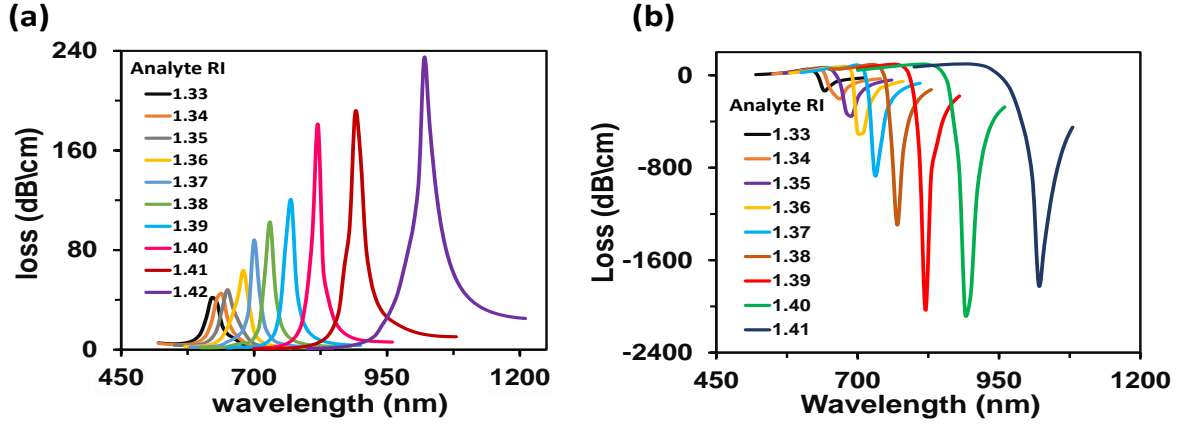


**Fig 4.6:** For single analyte sensing while both channels are filled by the same analyte (a) Loss spectrum with the change of analyte RI variation from  $n_a = 1.33$  to 1.42, and (b) amplitude sensitivities.

The results of single analyte detection using each sensing approach are shown in Table 2. From Table 1 we can observe that the wavelength sensitivities have not much changed, the SPR wavelength has changed by 1 nm, and the amplitude sensitivity has decreased. Consequently, the decreased amplitude sensitivities restrict the sensing effectiveness of the one channel injected method for detecting one analyte at a time. However, fiber-based sensors have a propensity to provide false-positive findings at times, and it is critical to eliminate these undesirable false responses. The single channel filled single RI sensing technique has minimal losses and may be used to identify false positive responses when sensitivity is not an issue. Furthermore, the signal-to-noise ratio (SNR) and detection limit (DL) are essential performance indicator factors. For the sensor, we use the following formulae to calculate the SNR and DL[71]

$$SNR = \frac{\Delta\lambda_{peak}}{\Delta\lambda_{\frac{1}{2}}}$$

$$DL = \frac{R}{S_\lambda}$$

Where DL represents the smallest quantity of analyte that the proposed sensor can properly  $\Delta\lambda_{peak}$  detect and peak represents the difference between resonant peaks.

**Table 3. Performance comparison of the proposed double D-shaped plasmonic sensor for multi-analyte detection.**

Structure types	Number of channels	Number of analytes	Material	Detected RI range	Wavelength sensitivity (nm/RIU)	Wavelength resolution (RIU)	Amplitude sensitivity (RIU <sup>-1</sup> )	Max. FOM	Max. LOD	Ref.
Wagon wheel fiber based sensor	3	2	Au	1.33-1.46	1,535 1,550	$6.50 \times 10^{-5}$ $6.50 \times 10^{-5}$	N/A	N/A	$4.2 \times 10^{-8}$	[56]
Double D-shaped PCF biosensor	4	2	Au Ag	1.33 - 1.366	2,500 3,083	$4.00 \times 10^{-5}$ $3.20 \times 10^{-5}$	N/A	N/A	$1.3 \times 10^{-8}$	[14]
Hybrid PCF based SPR sensor	2	2	Au	1.33-1.40 1.33-1.39	12,000 10,000	$8.33 \times 10^{-6}$ $1.00 \times 10^{-5}$	807 569	200	$7.0 \times 10^{-10}$	[4]
Duale channel-based PCF sensor	2	2	Au	1.40-1.41	4,400 3,500	$2.27 \times 10^{-5}$ $2.86 \times 10^{-5}$	N/A	N/A	$6.5 \times 10^{-9}$	[49]
Two-channels PCF biosensor	2	2	Au	1.33-1.35	7,500 2,500	$2.10 \times 10^{-5}$ $2.33 \times 10^{-5}$	N/A	N/A	$2.8 \times 10^{-9}$	[20]
Dual channel PCF sensor	2	2	Au	1.33–1.40	1000 3750	$1 \times 10^{-4}$ $2.6 \times 10^{-5}$	N/A	N/A	N/A	[13]
Graphene based D-shaped plasmonic sensor	2	2	Au	1.33-1.42	13000 13,000	$7.7 \times 10^{-6}$ $7.7 \times 10^{-6}$	2291 2063	481		This work

#### 4.4 Sensor tolerance & optimization

Parameter optimization is an essential step to obtain the best sensing response from a sensor. The proposed sensor is optimized by calibrating both channels using the identical analyte RI of 1.40. Impacts of Au layer thickness (t) variation on confinement loss and resonant peaks relocation are shown in Fig. 4.7 (a), and effects on amplitude sensitivity when analyte RI varies from 1.40 to 1.41 are depicted in Fig. 4.2 (b).

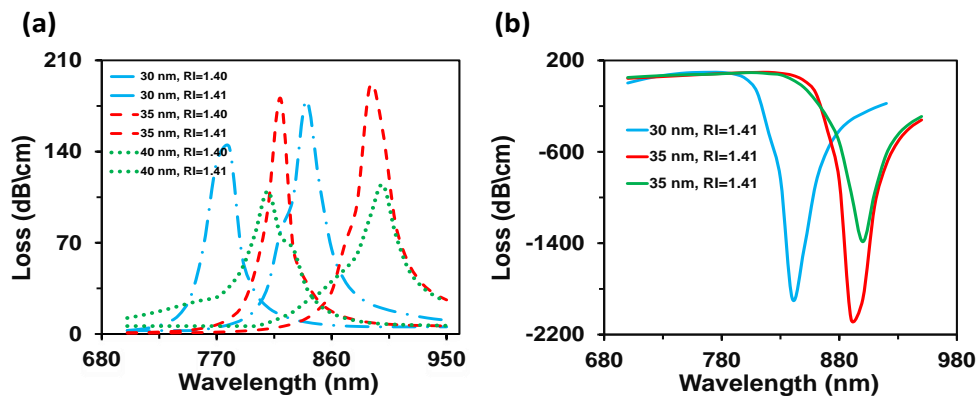


**Fig 4.7:** (a) Loss curves resulted from gold layer thickness variation and (b) relevant amplitude sensitivities.

Transmission losses are reduced and the resonant peaks shift further forward when the Au thickness increases, as seen in Fig. 4.7(a). The confinement losses of the sensor are 143 dB/cm for RI = 1.40 and 179 dB/cm for RI = 1.41 at  $t = 30$  nm. For every 0.01 change in RI, the resonant wavelength shifts from 780 nm to 840 nm. Propagation losses of 181 and 190 dB/cm are observed at resonance wavelengths of 820 and 890 nm, respectively, with a thickness of 35 nm. Peaks develop at 810 nm and 900 nm when the Au film thickness is 40 nm, indicating further loss depth degradation. Intensified plasmonic layer thickness leads to corresponding phase shifts of resonant wavelengths due to increased effective modal index. In contrast, substantial losses are generated by a thinner Au layer because more light may pass through it and couple with the sensing medium. As illustrated in Fig 4.7(b), a thin metal layer may display improved amplitude sensitivity. When the Au nano-layer is fattened from 30 nm to 35 nm, the sensitivity declines from 1886 RIU-1 to 2062 RIU-1 at analyte RI 1.41, as shown in Fig. 4.7(b). As a result, we choose 35 nm as the ideal Au layer thickness. We considered production tolerances in order to enhance operational efficiency.

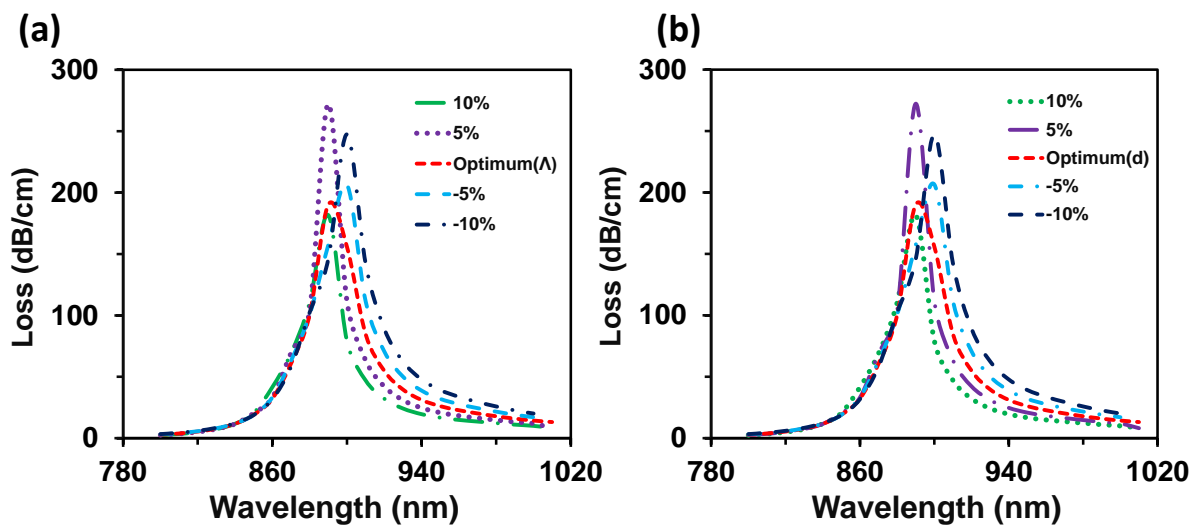


**Fig 4.8:** Tolerance investigation by changing (a) pitch size ( $\Lambda=2.028\mu\text{m}$ ) and (b) airholes diameter ( $d=1.95\mu\text{m}$ ).

The transmission loss varies with pitch size ( $\Lambda$ ) at RI = 1.41, as seen in Fig. 4.8(a). In the worst-case scenario, the sensor exhibits a modest resonant wavelength dislocation of 3 nm for a  $\pm 10$  deviation in the pitch from the optimal value (2.028 m). For a pitch size of 10% of the ideal value, the confinement loss increases to 247 dB/cm, and for a pitch size of -5%, the confinement loss decreases to 46 dB/cm. The spectrum of losses is shown to diminish progressively with increasing pitch sizes and vice versa. Therefore, the pitch size may be used

as a controllable parameter in SPR characteristics. The ideal value (1.95  $\mu\text{m}$ ) is seen for the big diameter (d) and has the sharpest propagation loss peak, as illustrated in Fig. 4.8. (b). Even a reduction in diameter by 10% and an increase in diameter by -5% from that selected size had little to no impact on the spectrum peaks and their independent placements.

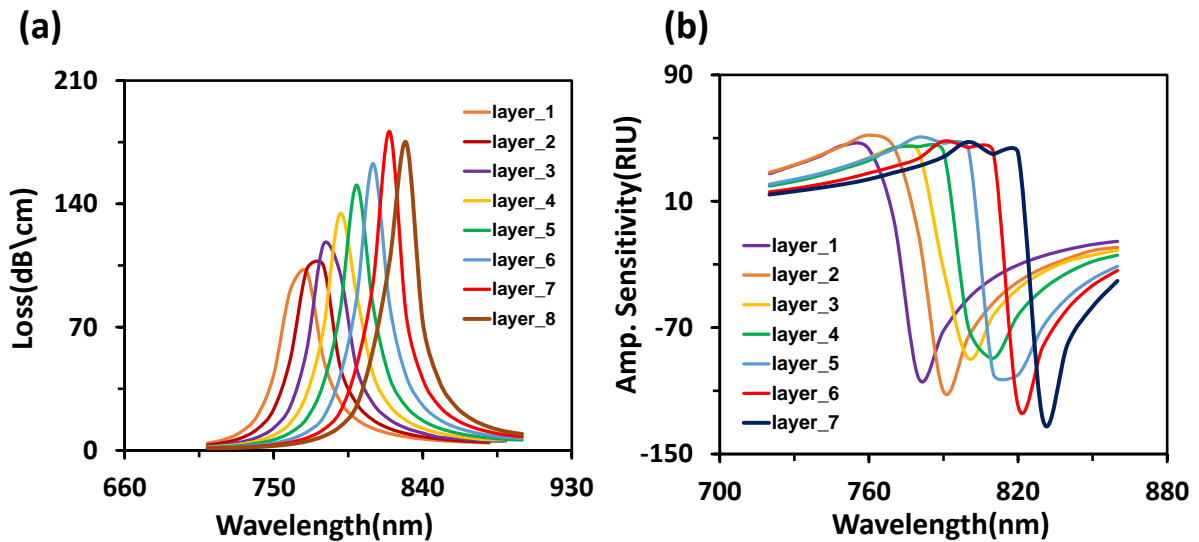


**Fig 4.9:** (a) Graphene layer variation of RI 1.41 (b) Amplitude sensitivity of Graphene layer

The ideal value (1.95  $\mu\text{m}$ ) is seen for the big diameter (d) and has the sharpest propagation loss peak, as illustrated in Fig. 4.8. (b). Even a reduction in diameter by 10% and an increase in diameter by -5% from that selected size had little to no impact on the spectrum peaks and their independent placements. Fig.4.9 shows the graphene layer variation where 4.9 (a) shows confinement loss and 4.9(b) shows the wavelength sensitivity.

## CHAPTER 5: CONCLUSION AND FUTURE WORK

### 5.1 Conclusion

We present a graphene-integrated, double-D shaped photonic crystal fiber (PCF) based plasmonic sensor for simultaneous detection of multi analytes. The typical stack-and-draw approach was used to create the double D-shaped PCF, and the SEM picture was used in the computational analyses. The D-shape was formed by etching down both the top and bottom surfaces of the fiber. The external sensing technique used by the double D-shaped structure facilitates a multi-analyte detection approach. Graphene's high surface-to-volume ratio enhances its sensing capabilities. The suggested sensor shows sensing phenomena for the x-polarized mode, and also reveals polarization dependence due to the asymmetry of the fiber structure. The sensor has a detection range of 1.33-1.42, within which it is able to detect the unknown analyte RI. To illustrate multi-analyte detection phenomena, the sensing range is split into two groups, Ch-1 (RI from 1.33 to 1.37) and Ch-2 (RI from 1.38 to 1.42). The sug sensor has a maximum wavelength sensitivity of 13,000 nm/RIU and an amplitude sensitivity of 2291 RIU-1.

### 5.2 Limitation

To create the proposed sensor, some limitations were taken into consideration throughout the design process. Even though the D-shaped sensor has a high sensing response, the research has some limitations. Specifically

1. To get a D shape in a fiber, precise polishing is necessary during fabrication.
2. When the distance between the core and the sensing channel is minimized, As a result the interaction of light with metal increases, leading to both high propagation loss and high sensitivity. The sensing length of the proposed sensor is reduced due to high propagation loss.
3. Only numerical analysis is used to determine how well a sensor is performing. We were unable to construct and characterize the suggested sensor due to a lack of appropriate manufacturing facilities.

### 5.3 Future Work

The use of PCFs in combination with SPR sensing technology is an exciting development in the field of biosensing. The literature assessment indicates that theoretical and numerical simulation form the backbone of the majority of the suggested work. Because of this, researchers are still trying to figure out how well each proposed sensor really works. To be sure, future efforts will focus on

1. Using an external sensing strategy in the design of a sensor may help cut down on both propagation loss and design complexity.
2. Making a PCF sensor and identifying its properties for use in experiments.
3. Performance comparison between the outcomes of the simulation and the findings of the experiment.

The SPR sensor based on PCF shows great promise for detecting chemical and biological analytes. As fabrication methods advance, researchers will explore more into PCF-based SPR sensor performance. The PCF based SPR sensor will soon be one of the most widely used optical biosensing technologies, with applications in medical diagnostics, food safety, liquid testing, environmental monitoring, and even security.

## REFERENCES

- [1] J. G. Ortega-Mendoza, A. Padilla-Vivanco, C. Toxqui-Quitl, P. Zaca-Morán, D. Villegas-Hernández, and F. Chávez, “Optical fiber sensor based on localized surface plasmon resonance using silver nanoparticles photodeposited on the optical fiber end,” *Sensors (Switzerland)*, vol. 14, no. 10, pp. 18701–18710, 2014, doi: 10.3390/s141018701.
- [2] D. G. Myszka, “Improving biosensor analysis,” *J. Mol. Recognit.*, vol. 12, no. 5, pp. 279–284, 1999, doi: 10.1002/(SICI)1099-1352(199909/10)12:5<279::AID-JMR473>3.0.CO;2-3.
- [3] V. Kaur and S. Singh, “Design of D-Shaped PCF-SPR sensor with dual coating of ITO and ZnO conducting metal oxide,” *Optik (Stuttg.)*, vol. 220, p. 165135, 2020, doi: 10.1016/j.ijleo.2020.165135.
- [4] S. Singh and Y. K. Prajapati, “TiO<sub>2</sub>/gold-graphene hybrid solid core SPR based PCF RI sensor for sensitivity enhancement,” *Optik (Stuttg.)*, vol. 224, no. June, p. 165525, 2020, doi: 10.1016/j.ijleo.2020.165525.
- [5] D. Pysz *et al.*, “Stack and draw fabrication of soft glass microstructured fiber optics,” *Bull. Polish Acad. Sci. Tech. Sci.*, vol. 62, no. 4, pp. 667–682, 2014, doi: 10.2478/bpasts-2014-0073.
- [6] N. Chen, M. Chang, X. Zhang, J. Zhou, X. Lu, and S. Zhuang, “Highly sensitive plasmonic sensor based on a dual-side polished photonic crystal fiber for component content sensing applications,” *Nanomaterials*, vol. 9, no. 11, 2019, doi: 10.3390/nano9111587.
- [7] S. Singh, S. K. Mishra, and B. D. Gupta, “SPR based fibre optic biosensor for phenolic compounds using immobilization of tyrosinase in polyacrylamide gel,” *Sensors Actuators, B Chem.*, vol. 186, pp. 388–395, 2013, doi: 10.1016/j.snb.2013.06.034.
- [8] A. K. Sharma, A. K. Pandey, and B. Kaur, “Fluoride fiber-based plasmonic biosensor with two-dimensional material heterostructures: Enhancement of overall figure-of-merit via optimization of radiation damping in near infrared region,” *Materials (Basel)*, vol. 12, no. 9, 2019, doi: 10.3390/ma12091542.

- [9] T. A. Birks, J. C. Knight, and P. S. J. Russell, “Endlessly single-mode photonic crystal fiber,” *Opt. Lett.*, vol. 22, no. 13, p. 961, 1997, doi: 10.1364/ol.22.000961.
- [10] A. A. Rifat, F. haider, R. Ahmed, G. A. Mahdiraji, F. R. Mahamd Adikan, and A. E. Miroschnichenko, “Highly sensitive selectively coated photonic crystal fiber-based plasmonic sensor,” *Opt. Lett.*, vol. 43, no. 4, p. 891, 2018, doi: 10.1364/ol.43.000891.
- [11] M. S. Islam *et al.*, “Dual-polarized highly sensitive plasmonic sensor in the visible to near-IR spectrum,” *Opt. Express*, vol. 26, no. 23, p. 30347, 2018, doi: 10.1364/oe.26.030347.
- [12] R. C. Jorgenson and S. S. Yee, “A fiber-optic chemical sensor based on surface plasmon resonance,” *Sensors Actuators B. Chem.*, vol. 12, no. 3, pp. 213–220, 1993, doi: 10.1016/0925-4005(93)80021-3.
- [13] A. A. Rifat, M. Rabiul Hasan, R. Ahmed, and A. E. Miroschnichenko, “Microstructured optical fiber-based plasmonic sensors,” *Comput. Photonic Sensors*, pp. 203–232, 2018, doi: 10.1007/978-3-319-76556-3\_9.
- [14] A. A. Rifat *et al.*, “Photonic crystal fiber based plasmonic sensors,” *Sensors Actuators, B Chem.*, vol. 243, pp. 311–325, 2017, doi: 10.1016/j.snb.2016.11.113.
- [15] V. Portosi, D. Laneve, M. C. Falconi, and F. Prudenzano, “Advances on photonic crystal fiber sensors and applications,” *Sensors (Switzerland)*, vol. 19, no. 8, 2019, doi: 10.3390/s19081892.
- [16] F. Haider, R. A. Aoni, R. Ahmed, W. J. Chew, and G. A. Mahdiraji, “Alphabetic-Core Assisted Microstructure Fiber Based Plasmonic Biosensor,” *Plasmonics*, vol. 15, no. 6, pp. 1949–1958, 2020, doi: 10.1007/s11468-020-01220-9.
- [17] A. Yasli, H. Ademgil, S. Haxha, and A. Aggoun, “Multi-Channel Photonic Crystal Fiber Based Surface Plasmon Resonance Sensor for Multi-Analyte Sensing,” *IEEE Photonics J.*, vol. 12, no. 1, 2020, doi: 10.1109/JPHOT.2019.2961110.
- [18] L. Xia, B. Shuai, W. Li, and D. Liu, “Polarization detection analysis of dual-channel surface plasmon resonance sensing for silicone oils based on the D-shaped fiber with a central hole,” *Opt. Commun.*, vol. 285, no. 18, pp. 3730–3734, 2012, doi: 10.1016/j.optcom.2012.05.001.



- [19] Y. Guo *et al.*, “Highly sensitive sensor based on D-shaped microstructure fiber with hollow core,” *Opt. Laser Technol.*, vol. 123, no. September 2019, p. 105922, 2020, doi: 10.1016/j.optlastec.2019.105922.
- [20] H. Lu *et al.*, “Graphene-based active slow surface plasmon polaritons,” *Sci. Rep.*, vol. 5, pp. 1–7, 2015, doi: 10.1038/srep08443.
- [21] W. L. Barnes, A. Dereux, and T. W. Ebbesen, “Surface plasmon subwavelength optics,” *Nature*, vol. 424, no. 6950, pp. 824–830, 2003, doi: 10.1038/nature01937.
- [22] M. Bonsignori *et al.*, “Staged induction of HIV-1 glycan-dependent broadly neutralizing antibodies,” *Sci. Transl. Med.*, vol. 9, no. 381, 2017, doi: 10.1126/scitranslmed.aai7514.
- [23] J. Homola, “Present and future of surface plasmon resonance biosensors,” *Anal. Bioanal. Chem.*, vol. 377, no. 3, pp. 528–539, 2003, doi: 10.1007/s00216-003-2101-0.
- [24] C. Republic, “Surface Plasmon Resonance ( SPR ) Sensors,” no. July, pp. 45–67, 2006.
- [25] A. Otto, “Excitation of nonradiative surface plasma waves in silver by the method of frustrated total reflection,” *Zeitschrift für Phys.*, vol. 216, no. 4, pp. 398–410, 1968, doi: 10.1007/BF01391532.
- [26] J. Homola, “Electromagnetic Theory of Surface Plasmons,” no. July, pp. 3–44, 2006, doi: 10.1007/5346\_013.
- [27] E. Kretschmann and H. Raether, “Radiative decay of non-radiative surface plasmons by light,” *Z. Naturforsch.*, vol. 23, no. a, pp. 2135–2136, 1968.
- [28] M. Couture, L. S. Live, A. Dhawan, and J. F. Masson, “EOT or Kretschmann configuration? Comparative study of the plasmonic modes in gold nanohole arrays,” *Analyst*, vol. 137, no. 18, pp. 4162–4170, 2012, doi: 10.1039/c2an35566c.
- [29] S. L. Jarvenpaa, K. Knoll, and D. E. Leidner, “Is anybody out there? Antecedents of trust in global virtual teams,” *J. Manag. Inf. Syst.*, vol. 14, no. 4, pp. 29–64, 1997, doi: 10.1080/07421222.1998.11518185.
- [30] S. S. Musa, S. Zhao, M. H. Wang, A. G. Habib, U. T. Mustapha, and D. He, “Estimation of exponential growth rate and basic reproduction number of the coronavirus disease 2019 (COVID-19) in Africa,” *Infect. Dis. Poverty*, vol. 9, no. 1, pp. 1–6, 2020, doi: 10.1186/s40249-020-00718-y.

- [31] N. Nisha, M. Iqbal, and A. Rifat, "The changing paradigm of health and mobile phones: An innovation in the health care system," *J. Glob. Inf. Manag.*, vol. 27, no. 1, pp. 19–46, 2019, doi: 10.4018/JGIM.2019010102.
- [32] G. Renversez, B. Kuhlmeij, and R. McPhedran, "Dispersion management with microstructured optical fibers: ultraflattened chromatic dispersion with low losses," *Opt. Lett.*, vol. 28, no. 12, p. 989, 2003, doi: 10.1364/ol.28.000989.
- [33] S. Jp, "(12) United States Patent," vol. 2, no. 12, 2009.
- [34] O. Publications, "(12) United States Patent," vol. 2, no. 12, pp. 12–17, 2006.
- [35] H. E. Joe, H. Yun, S. H. Jo, M. B. G. Jun, and B. K. Min, "A review on optical fiber sensors for environmental monitoring," *Int. J. Precis. Eng. Manuf. - Green Technol.*, vol. 5, no. 1, pp. 173–191, 2018, doi: 10.1007/s40684-018-0017-6.
- [36] Z. Huang, W. Xu, and K. Yu, "Bidirectional LSTM-CRF Models for Sequence Tagging," 2015, [Online]. Available: <http://arxiv.org/abs/1508.01991>
- [37] A. M. Arangio, H. Tong, J. Socorro, U. Pöschl, and M. Shiraiwa, "Quantification of environmentally persistent free radicals and reactive oxygen species in atmospheric aerosol particles," *Atmos. Chem. Phys.*, vol. 16, no. 20, pp. 13105–13119, 2016, doi: 10.5194/acp-16-13105-2016.
- [38] D. Noordegraaf, P. M. Skovgaard, M. D. Nielsen, and J. Bland-Hawthorn, "Efficient multi-mode to single-mode coupling in a photonic lantern," *Opt. Express*, vol. 17, no. 3, p. 1988, 2009, doi: 10.1364/oe.17.001988.
- [39] J. C. Knight, T. A. Birks, P. S. J. Russell, and D. M. Atkin, "All-silica single-mode optical fiber with photonic crystal cladding: errata," *Opt. Lett.*, vol. 22, no. 7, p. 484, 1997, doi: 10.1364/ol.22.000484.
- [40] J. C. Knight, J. Broeng, T. A. Birks, and P. S. J. Russell, "Photonic band gap guidance in optical fibers," *Science (80-. )*, vol. 282, no. 5393, pp. 1476–1478, 1998, doi: 10.1126/science.282.5393.1476.
- [41] T. Gissibl, M. Vieweg, M. M. Vogel, M. Aboud Ahmed, T. Graf, and H. Giessen, "Preparation and characterization of a large mode area liquid-filled photonic crystal fiber: Transition from isolated to coupled spatial modes," *Appl. Phys. B Lasers Opt.*,

- vol. 106, no. 3, pp. 521–527, 2012, doi: 10.1007/s00340-011-4859-7.
- [42] D. C. Zografopoulos, A. Ptilakis, and E. E. Kriezis, “Liquid crystal-infiltrated photonic crystal fibres for switching applications,” *Optofluidics, Sensors Actuators Microstruct. Opt. Fibers*, pp. 55–83, 2015, doi: 10.1016/B978-1-78242-329-4.00003-5.
- [43] X. Wang, Q. Wang, Z. Song, and K. Qi, “Simulation of a microstructure fiber pressure sensor based on lossy mode resonance,” *AIP Adv.*, vol. 9, no. 9, 2019, doi: 10.1063/1.5112090.
- [44] M. Al Mahfuz, M. A. Hossain, E. Haque, N. H. Hai, Y. Namihira, and F. Ahmed, “A bimetallic-coated, low propagation loss, photonic crystal fiber based plasmonic refractive index sensor,” *Sensors (Switzerland)*, vol. 19, no. 17, 2019, doi: 10.3390/s19173794.
- [45] F. Haider *et al.*, “Multi-Analyte Detection Based on Integrated Internal and External Sensing Approach,” *IEEE Trans. Nanobioscience*, vol. 21, no. 1, pp. 29–36, 2022, doi: 10.1109/TNB.2021.3108834.
- [46] M. R. Hasan *et al.*, “Spiral photonic crystal fiber-based dual-polarized surface plasmon resonance biosensor,” *IEEE Sens. J.*, vol. 18, no. 1, pp. 133–140, 2018, doi: 10.1109/JSEN.2017.2769720.
- [47] S. B. Gokturk, H. Yalcin, and C. Bamji, “A time-of-flight depth sensor - System description, issues and solutions,” *IEEE Comput. Soc. Conf. Comput. Vis. Pattern Recognit. Work.*, vol. 2004-Janua, no. January, 2004, doi: 10.1109/CVPR.2004.291.
- [48] E. Haque, S. Mahmuda, M. A. Hossain, N. H. Hai, Y. Namihira, and F. Ahmed, “Highly sensitive dual-core PCF based plasmonic refractive index sensor for low refractive index detection,” *IEEE Photonics J.*, vol. 11, no. 5, pp. 1–9, 2019, doi: 10.1109/JPHOT.2019.2931713.
- [49] G. Ghosh, “Dispersion-equation coefficients for the refractive index and birefringence of calcite and quartz crystals,” *Opt. Commun.*, vol. 163, no. 1, pp. 95–102, 1999, doi: 10.1016/S0030-4018(99)00091-7.
- [50] A. Hassani and M. Skorobogatiy, “Design of the microstructured optical fiber-based surface plasmon resonance sensors with enhanced microfluidics,” *Opt. Express*, vol. 14, no. 24, p. 11616, 2006, doi: 10.1364/oe.14.011616.

- [51] J. Gao, S. P. Sun, W. P. Zhu, and T. S. Chung, “Chelating polymer modified P84 nanofiltration (NF) hollow fiber membranes for high efficient heavy metal removal,” *Water Res.*, vol. 63, pp. 252–261, 2014, doi: 10.1016/j.watres.2014.06.006.
- [52] A. A. Rifat *et al.*, “Surface Plasmon Resonance Photonic Crystal Fiber Biosensor: A Practical Sensing Approach,” *IEEE Photonics Technol. Lett.*, vol. 27, no. 15, pp. 1628–1631, 2015, doi: 10.1109/LPT.2015.2432812.
- [53] V. Kaur and S. Singh, “A dual-channel surface plasmon resonance biosensor based on a photonic crystal fiber for multianalyte sensing,” *J. Comput. Electron.*, vol. 18, no. 1, pp. 319–328, 2019, doi: 10.1007/s10825-019-01305-7.
- [54] C. Zhou *et al.*, “Highly efficient base editing in human tripronuclear zygotes,” *Protein Cell*, vol. 8, no. 10, pp. 772–775, 2017, doi: 10.1007/s13238-017-0459-6.
- [55] B. H. Almewafy, N. F. F. Areed, M. F. O. Hameed, and S. S. A. Obayya, “Modified D-shaped SPR PCF polarization filter at telecommunication wavelengths,” *Opt. Quantum Electron.*, vol. 51, no. 6, 2019, doi: 10.1007/s11082-019-1885-x.
- [56] Y. Zhang, C. Zhou, L. Xia, X. Yu, and D. Liu, “Wagon wheel fiber based multichannel plasmonic sensor,” *Opt. Express*, vol. 19, no. 23, p. 22863, 2011, doi: 10.1364/oe.19.022863.
- [57] R. Otupiri, E. K. Akowuah, and S. Haxha, “Multi-channel SPR biosensor based on PCF for multi-analyte sensing applications,” *Opt. Express*, vol. 23, no. 12, p. 15716, 2015, doi: 10.1364/oe.23.015716.
- [58] J. N. Dash and R. Jha, “Graphene-based birefringent photonic crystal fiber sensor using surface plasmon resonance,” *IEEE Photonics Technol. Lett.*, vol. 26, no. 11, pp. 1092–1095, 2014, doi: 10.1109/LPT.2014.2315233.
- [59] M. F. O. Hameed, Y. K. A. Alrayk, A. A. Shaalan, W. S. El Deeb, and S. S. A. Obayya, “Design of highly sensitive multichannel bimetallic photonic crystal fiber biosensor,” *J. Nanophotonics*, vol. 10, no. 4, p. 046016, 2016, doi: 10.1117/1.jnp.10.046016.
- [60] G. W. Hanson, “Dyadic Green’s functions and guided surface waves for a surface conductivity model of graphene,” *J. Appl. Phys.*, vol. 103, no. 6, 2008, doi: 10.1063/1.2891452.

- [61] M. Piliarik, J. Homola, Z. Maníková, and J. Čtyroký, “Surface plasmon resonance sensor based on a single-mode polarization-maintaining optical fiber,” *Sensors Actuators, B Chem.*, vol. 90, no. 1–3, pp. 236–242, 2003, doi: 10.1016/S0925-4005(03)00034-0.
- [62] P. O. Patil *et al.*, “Graphene-based nanocomposites for sensitivity enhancement of surface plasmon resonance sensor for biological and chemical sensing: A review,” *Biosens. Bioelectron.*, vol. 139, p. 111324, 2019, doi: 10.1016/j.bios.2019.111324.
- [63] L. Zhao, H. Han, Y. Lian, N. Luan, and J. Liu, “Theoretical analysis of all-solid D-type photonic crystal fiber based plasmonic sensor for refractive index and temperature sensing,” *Opt. Fiber Technol.*, vol. 50, no. February, pp. 165–171, 2019, doi: 10.1016/j.yofte.2019.03.013.
- [64] N. Luan, L. Zhao, Y. Lian, and S. Lou, “A high refractive index plasmonic sensor based on d-shaped photonic crystal fiber with laterally accessible hollow-core,” *IEEE Photonics J.*, vol. 10, no. 5, pp. 1–7, 2018, doi: 10.1109/JPHOT.2018.2873826.
- [65] V. S. Gangwar, A. K. Singh, and S. P. Singh, “An Effective Approach for the Synthesis of Unequally Spaced Antenna Array by Estimating Optimum Elements Density on the Aperture,” *IEEE Antennas Wirel. Propag. Lett.*, vol. 16, no. c, pp. 2278–2282, 2017, doi: 10.1109/LAWP.2017.2714182.
- [66] T. Wu *et al.*, “Surface plasmon resonance biosensor based on gold-coated side-polished hexagonal structure photonic crystal fiber,” *Opt. Express*, vol. 25, no. 17, p. 20313, 2017, doi: 10.1364/oe.25.020313.
- [67] L. Souqui, J. Palisaitis, H. Högberg, and H. Pedersen, “Plasma CVD of B-C-N thin films using triethylboron in argon-nitrogen plasma,” *J. Mater. Chem. C*, vol. 8, no. 12, pp. 4112–4123, 2020, doi: 10.1039/d0tc00616e.
- [68] D. Gao, C. Guan, Y. Wen, X. Zhong, and L. Yuan, “Multi-hole fiber based surface plasmon resonance sensor operated at near-infrared wavelengths,” *Opt. Commun.*, vol. 313, pp. 94–98, 2014, doi: 10.1016/j.optcom.2013.10.015.
- [69] A. Islam, F. Haider, R. Ahmmed Aoni, M. Hossen, F. Begum, and R. Ahmed, “U-grooved dual-channel plasmonic sensor for simultaneous multi-analyte detection,” *J. Opt. Soc. Am. B*, vol. 38, no. 10, p. 3055, 2021, doi: 10.1364/josab.435255.
- [70] P. Bing *et al.*, “Analysis of Dual-Channel Simultaneous Detection of Photonic Crystal

Fiber Sensors,” *Plasmonics*, vol. 15, no. 4, pp. 1071–1076, 2020, doi: 10.1007/s11468-020-01131-9.

- [71] M. Mahabubur Rahman, M. Aslam Molla, A. Kumar Paul, M. A. Based, M. Masud Rana, and M. S. Anower, “Numerical investigation of a highly sensitive plasmonic refractive index sensor utilizing hexagonal lattice of photonic crystal fiber,” *Results Phys.*, vol. 18, p. 103313, 2020, doi: 10.1016/j.rinp.2020.103313.